



Faculty of Science

PC5286 Master Project Final Report

First-principles studies of quantum defect candidates in 2D WS₂

Ning Siyuan

(Student ID: E1127489)

Supervised by:

Prof. QUEK Su Ying

Content

1 Introduction	1
2 Solid-state Quantum Defect.....	2
2.1 Defect Centers in Diamond.....	4
2.1.1 NV Center	4
2.1.2 Split-vacancy Color Centers	8
2.2 Defect Centers in SiC	9
2.3 Defect Centers Hosted in 2D Materials:	12
2.3.1 Hexagonal Boron Nitride	14
2.3.2 Transition metal dichalcogenides	18
2.4 Other Potential Host Materials	23
2.4.1 Zinc Oxide.....	23
2.4.2 Gallium Nitride	24
2.4.3 Real-earth Materials	25
3 Key Quantities and DFT Approaches.....	26
3.1 Crystal Symmetry.....	30
3.2 Formation Energy and Charge Transition Level	35
3.3 Zero Field Splitting.....	40
4 First-principles studies of quantum defects in 2D WS ₂	43
4.1 Defect Supercell.....	43
4.2 Defect Formation Energy.....	46
4.2.1 Chemical Potential Feasible Region.....	46
4.2.2 Charge Correction	52
4.2.3 Formation Energies and Charge Transition Level.....	54
4.3 Spin-triplet Ground State	56
5 Summary	58
6 Reference	59

1 Introduction

Defects commonly exist in all materials and significantly alter their electrical, optical, and mechanical characteristics. These alterations enable a broad spectrum of tunable responses and introduce novel functionalities crucial for devices like transistors and lasers. When isolated, defects function similarly to entrapped atoms or molecules, embodying discrete electronic states within the band gap of the host material, referred to as the semiconductor vacuum¹. These states possess controllable orbital and spin degrees of freedom via electromagnetic fields.

In specific configurations, the electron and nuclear orbital or spin degrees of freedom linked to defects can be sufficiently shielded from environmental disruptions, such as thermal phonons, electromagnetic interference, free carriers, and other material defects. This isolation allows the preparation and preservation of quantum-mechanical superpositions of these states for durations conducive to their application in quantum information science.

Point defects that isolate within the host materials mimic atoms and exhibit quantum characteristics determined by their charge and spin states, including optical transitions. These defects, termed **quantum point defects (QPD)**^{2,3}, serve as a prime framework for harnessing quantum mechanical principles to surpass traditional functionalities and techniques⁴. The primary applications of interest include single photon emitters (SPE), spin qubits, and quantum sensing, as illustrated in Fig. 1.1. SPEs operate as quantum systems that emit a single photon per excitation cycle when activated optically or electrically. Another frequently discussed concept is photon-spin interfaces (PSI), where electronic spins are initialized, manipulated, and read via photons to establish a durable spin memory.

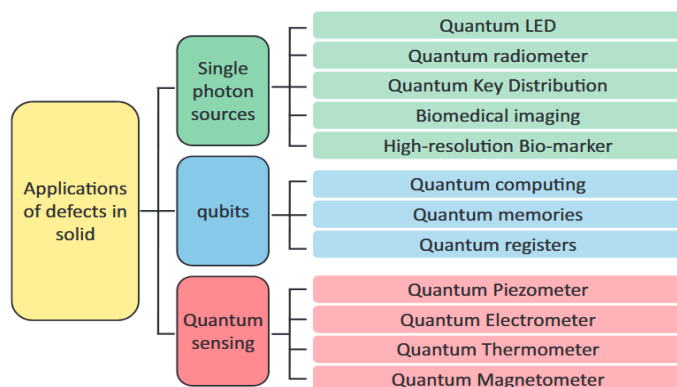


Fig. 1.1 The major applications of defects in solids².

2 Solid-state Quantum Defect

The diamond NV centers in diamond (Fig. 2.1A) stands as the prototype and most thoroughly investigated QPDs. The drive to discover spin qubits boasting enhanced properties and novel functionalities has inspired extensive research into semiconductor defects. Recent explorations have expanded to include diverse systems in diamond (refer to Fig. 2.1B) and SiC (refer to Fig. 2.1C), as well as examining rare-earth ions in oxide II–VI and III–V compounds (see Fig. 2.1D), encompassing materials like ZnO ⁵ and GaN ⁶. Investigations also extend to low-dimensional structures such as the transition metal dichalcogenide (TMD) WSe2 ⁷ and hexagonal boron nitride (hBN)⁸. While theoretical insights into many of these systems remain incomplete, and the chemical structures of some defects are yet to be determined, these materials demonstrate potential superiorities over NV centers. They exhibit properties such as optical indistinguishability, heightened luminosity, enhanced functionality in nanophotonic devices^{9,10}, and compatibility with advanced semiconductor hosts¹¹. Also, The quantum confinement effect causes the semiconductor bandgap to widen as the dimensions of the crystals decrease. Consequently, even though narrow bandgap semiconductors are typically not optimal for

hosting deep centers, their nano-sized versions emerge as viable candidates for operations at elevated temperatures.

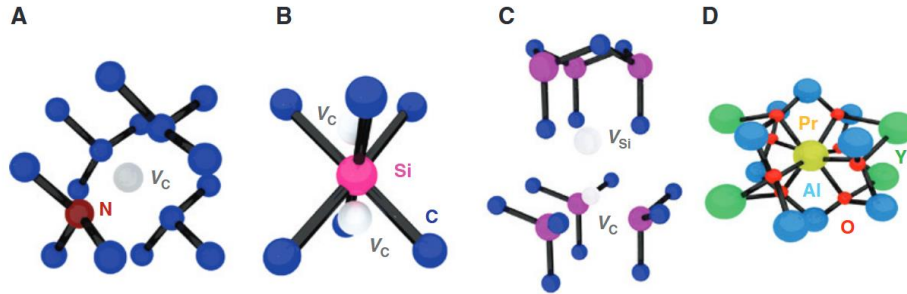


Fig. 2.1 Prominent quantum point defects. (A) Nitrogen-vacancy center in diamond; (B) silicon-vacancy center in diamond; (C) divacancy in 4H-SiC; and (D) substitutional Pr ion in yttrium aluminum garnet (YAG)³.

A primary benefit of solid-state qubits is their compatibility with existing microelectronic frameworks¹². Although diamond exhibits desirable optical properties at room temperature for defect qubits, its growth at wafer scale and subsequent semiconductor device fabrication remain challenging. This limitation has driven the search for alternative materials that harbor atomic-scale defects. These alternatives aim to replicate the advantageous coherence and readout characteristics akin to those of the diamond NV center. The selection of suitable host materials and defect states is subject to specific constraints, thoroughly discussed. Here, it is noted that while wide bandgap materials¹³ are preferred for hosting well-defined atomic-scale defect states due to their suitability for optical readout, materials with moderate or smaller bandgaps also hold significant promise, especially when operated at low temperatures.

2.1 Defect Centers in Diamond

2.1.1 NV Center

Structurally, the NV center is characterized as a point defect in diamond where a nitrogen atom replaces a carbon atom adjacent to a vacancy, potentially trapping an extra electron to form an NV(-) defect. The electronic structure of the NV⁻ center, depicted in Fig. 2.2, reveals that the ground-state electron occupation of the negative charge state¹⁴ comprises two singly degenerate states with a_1 symmetry, both filled (the lower aligning with the valence band), and a half-filled doubly degenerate state with e symmetry. This configuration results in a triplet ground state of 3A_2 . The magnetic sublevels $m_s = 0$ and $m_s = \pm 1$ exhibit a zero-field splitting (ZFS) of $D = 2.88\text{GHz}$. Upon optical excitation to the 3E state, an electron transitions from the upper a_1 state to an empty e state, with the zero-phonon line (ZPL) of this transition at 1.945eV (637 nm). The excited state, similar in magnetic structure to the ground state, has a ZFS of $D = 1.42\text{GHz}$ (9) at room temperature. This excitation process predominantly preserves spin states, linking the $m_s = 0$ level of the ground state to the corresponding $m_s = 0$ level of the excited state and similarly for $m_s = \pm 1$ levels.

Besides the triplet states, there exist two low-lying singlet states, 1A_1 and 1E . If the system is initially in the $m_s = 0$ level of the excited 3E state, it returns to the ground state via emission of a photon with a lifetime of $\sim 13\text{ ns}$. However, for the $m_s = \pm 1$ states there is a comparable probability for the so-called intersystem crossing (ISC), whereby the NV⁻ center transitions into the singlet 1A_1 state. After that, there is a very fast (lifetime $\sim 1\text{ ns}$, mostly nonradiative) transition to the lower-lying 1E state. This is a relatively long-lived metastable state [lifetime of $\sim 150\text{ ns}$ at room temperature]. From here the system undergoes another ISC to the triplet 3A_2 state, predominantly coupling to the $m_s = 0$

sublevel. After a few such cycles, the NV^- center can be initialized into the $m_s = 0$ spin state, which can then be controlled using microwaves. The electronic structure of the NV^- center thus enables optical spin initialization. Conveniently, it also allows for optical spin readout, as the luminescence intensity now depends on the spin state. The above-described mechanism of spin initialization and readout has been understood after many years of experimental research, with the upper ISC put on firm theoretical ground¹⁵

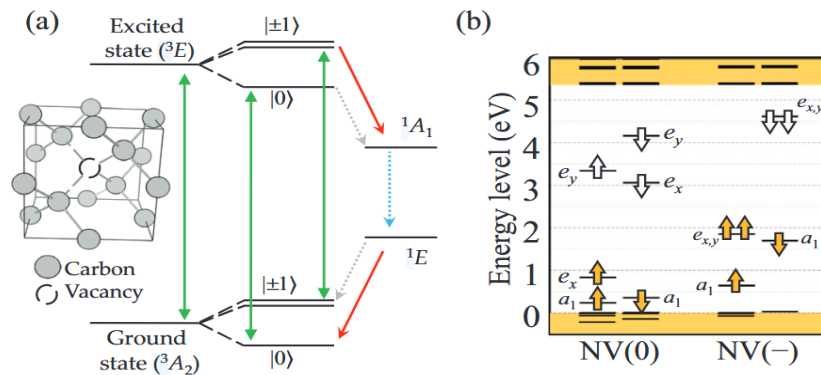


Fig. 2.2 (a) Structure of an NV center in diamond and its energy level diagram in an optical polarization cycle. The green arrows represent the spin-conserving absorption and emission; dotted and red straight arrows represent the weak and efficient intersystem crossings, respectively, and the cyan dotted arrow represents a weak near-infrared emission competing with the direct non-radiative decay. The excited state level diagram is simplified to the case of elevated temperatures. (b) The ground state of single particle NV defect energy levels in the fundamental bandgap of diamond. Filled and empty arrows depict the occupied (electron) and unoccupied (hole) states, respectively, as found in spin-polarized density functional theory calculations¹⁵.

Substantial studies on the fundamental properties and working mechanism of the NV center have been conducted. The electronic spin state of NV centers can be initialized, manipulated, and detected at room temperature through optical pumping, microwave spin resonance, and photoluminescence, respectively¹⁶. The susceptibility of these spins to nearby fields such as electric, magnetic, thermal,

and strain fields, combined with the capability to integrate these defects into nanostructures, introduces innovative approaches to nanoscale sensing across physics, chemistry, and biology¹⁷. Additionally, each NV center acts as a quantum register composed of electron and nuclear spins, which can be individually controlled, entangled, and maintained coherently for extended periods¹⁸, facilitating quantum operations such as teleportation and error correction. The temperature dependence of the optical transition linewidth and excited state relaxation of a single NV center were associated with strong electron–phonon coupling. At temperatures of liquid helium, NV center electronic spins coherently interact with light and can be entangled remotely via photonic channels¹⁸, laying the groundwork for expansive quantum networks¹⁹.

L.C. Bassett and co-workers³ provide a brief historical review to demonstrate how our comprehension of quantum defects, the push towards specific quantum technologies, and material developments interplay within the QPD domain. Based on NV-center-based systems, Table 2.1 presents the connection between a physical property of a QPD, the physics behind the property, the challenges it presents, and the opportunities it enables, with respect to mitigating the challenges and enabling new applications. The existing works on NV centers offers valuable insights for the discovery of new quantum defects.

Property	Physics	Challenges	Mitigations	Applications
Inter-system crossing (ISC)	Spin-orbit coupling, phonon interactions, excited state structure	Spin-readout SNR	Alternative readout strategies	Optical readout
Ground-state response to local fields	Ground-state electronic structure	Inhomogeneous broadening, sensor stability	Double quantum magnetometry, active control	Sensors

Property	Physics	Challenges	Mitigations	Applications
Phonon-assisted/ phonon- broadened transitions	Excited-state structure, Jahn-Teller interactions	Photon indistinguishability, ZPL efficiency	Photonic cavities	Off-resonant spin readout, thermometry
¹³ C nuclear bath	Central spin model, non-Markovian dynamics	Spin decoherence	Isotope purification dynamic decoupling	Qubit registers
Multiple charge states	Charge capture, nonlinear and non- equilibrium effects	Stabilization of desired charge state	Optical charge control Fermi-level control	Enhanced readout schemes

Tab. 2.1 The realtions of Properties, physics, challenges, mitigations, applications based on NV centers³.

Over the past two decades, the quantum control techniques for NV center spins have succeeded in the precision manipulation of single spins. Current research is primarily aimed at advancing coherent control of multiple quantum states—a common objective across in quantum computing. Weakly coupled nuclear spins adjacent to NV centers are being explored as potential multi-qubit systems. Additionally, hybrid systems combining NV center electron spins with photonic qubits or superconducting qubits are proving promising, achieving several breakthroughs recently. Diamond color centers have emerged as a leading solid-state platform for advancing quantum technologies. For instance, recent developments have showcased quantum advantages in key distribution, highlighted by Linsen Li and Dirk Englund ²⁰ who have developed a modular quantum system-on-chip (QSoC) architecture. This system integrates thousands of individually addressable tin vacancy spin qubits within a two-dimensional array on a quantum microchip, operated under cryogenic conditions.

2.1.2 Split-vacancy Color Centers

The silicon-vacancy (SiV) defect in diamond, characterized by an interstitial silicon atom in a split-vacancy configuration, belongs to the D_{3d} symmetry group. This configuration results in ground (2E_g) and excited (2E_u) electronic states, both exhibiting double orbital degeneracy. Utilizing group theory and advanced ab initio methods, Gali and Maze²¹ analyzed the electronic structure of this defect, noting the central position of the silicon atom in a bond between two adjacent vacancies—an arrangement also known as the V–Si–V defect. Both states are susceptible to the Jahn-Teller effect, significantly affecting photon emission due to electron-phonon interactions, with linewidths that vary with temperature; increasing cubically between 70 K and 350 K and linearly below 20 K²².

The SiV(-) defect offers advantages such as narrow inhomogeneous linewidth and stability against electric field noise, but is hindered by low quantum efficiencies (around 10%) and short coherence times at low temperatures. These limitations have prompted the exploration of other quantum emitters like group-IV vacancy color centers XV, where X includes Si, Ge, Sn, and Pb. These heavier centers, such as GeV, SnV, and PbV, share similar geometric structures with SiV but exhibit larger spin-orbit coupling, potentially enhancing spin coherence times. These defects demonstrate strong electron-phonon coupling due to significant Jahn–Teller interactions in their orbital structures²³. Recent research has focused particularly on the optical and spin properties of SnV centers, which are being intensively studied for their high-temperature operation capabilities after processes like high-temperature annealing or chemical vapor deposition (CVD) post-Sn implantation^{24,25}. Alternative methods such as microwave plasma CVD have been employed to integrate these centers into diamond, offering high-quality crystals though without precise control over defect positioning.

While diamond exhibits satisfying optical properties at room temperature, scaling its growth to wafer dimensions and fabricating semiconductor devices from it are complex processes. The positions of diamond hosted defects are hard to precisely control in nanoscale, resulting in inefficient device fabrication and performance that often falls short of expectations. The primary challenge lies in aligning the NV center creation process with the diamond etching process²⁶. These challenges have spurred the search for alternative materials and atomic-scale defects that offer robustness and ease of control comparable to the NV center, yet with similar coherence and readout capabilities. Such requirements determine the selection of suitable host materials and the types of defect states that can be effectively utilized.

2.2 Defect Centers in SiC

Inspired by the color centers in diamond, deep color centers have been considered in other host crystals. Weber et al. outlined essential physical criteria for potential color centers and their hosts²⁷, identifying silicon carbide (SiC) as a promising candidate due to its large bandgap and minimal nuclear spin concentration. This choice aligns with theoretical predictions that highlighted divacancy defects in SiC as viable alternatives to the NV center in diamond²⁸. SiC features a hexagonal lattice structure, with bilayers arranged in quasi-hexagonal (h) or quasi-cubic (k) formations. This structure gives rise to over 200 polytypes of SiC, such as 3C, 4H, and 6H, noted in Ramsdell notation with bandgaps of 2.4 eV, 3.2 eV, and 3.0 eV, respectively. The 4H-SiC polytype, in particular, is extensively used in modern semiconductor technologies, including the production of high-quality 4-inch wafers that facilitate controlled doping processes aimed at reducing costs in future SiC-based quantum devices. In 4H-SiC, alternating h and k bilayers lead to diverse defect configurations, including monovacancies and more complex divacancies. These configurations not only complicate

defect identification but also offer the potential to simultaneously produce multiple qubits with distinct yet comparable properties.

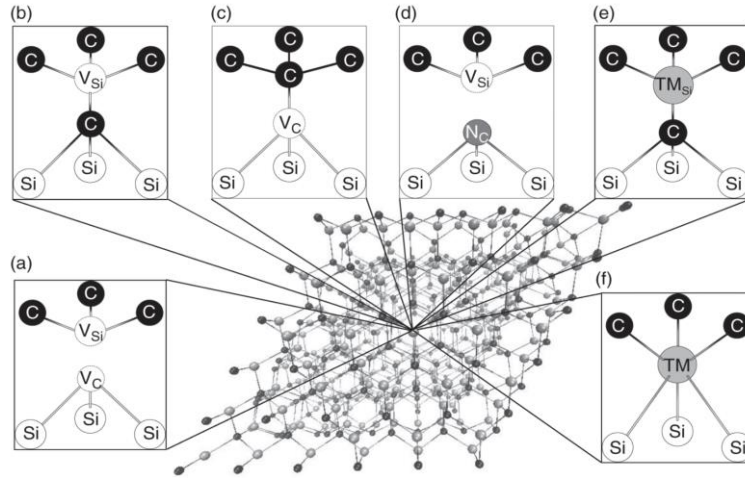


Fig. 2.3 Typical defects in SiC. TM stands for transition metal ion, whereas V and V_C labels the Si-vacancy and C-vacancy, respectively⁸.

Potential defect types in SiC have been presented in Fig. 2.3. Notably, the divacancies in SiC have spin levels sensitive to strain, electric fields, magnetic field, and temperature, which can potentially be harnessed in quantum application. One prominent divacancy is the neutral divacancy $(V_C - V_{Si})^0$, for which a number of impressive advances, including the detection of single centers with millisecond coherence times, have been demonstrated. Nitrogen-vacancy pair defects ($N_C V_{Si}$) have recently been observed in N-doped 3C, 4H, and 6H-SiC polytype crystals. The negatively charged $N_C V_{Si}$ show broad photoluminescence spectra and NIR emission arising from the transition between the 3E excited and 3A_2 ground states, both of which exhibit $S = 1$ spin states²⁹.

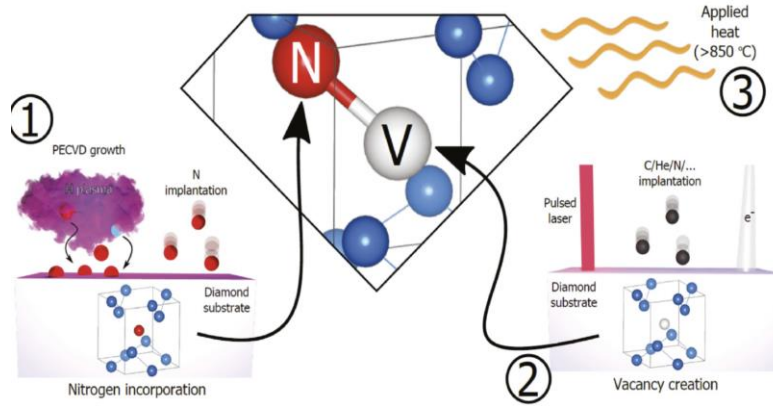


Fig. 2.4 Processes involved in the generation of the nitrogen-vacancy colour centres in diamond ³⁰

The primary advantage of SiC host lies in its mature fabrication techniques. The semiconductor industry extensively utilizes high-quality 4H-SiC wafers, with developed well-controlled doping technologies. Thus, future SiC-based quantum devices can hold reduced production cost and established process to be integrated. Indeed, both single divacancy and silicon-vacancy spins have been successfully integrated and manipulated within SiC diode structures. Moreover, individual SiC spins have the potential to be incorporated into photonic structures, paving the way for the next generation of quantum optoelectronic devices. While 4H-SiC's bandgap is smaller than diamond's at 3.3 eV, it is sufficiently large to accommodate near-infrared (NIR) quantum emitters, which are particularly beneficial for applications in quantum sensing for biology and quantum communications. However, the relatively narrow energy spacing between defect levels and the significantly lower Debye temperature of 4H-SiC (approximately 1000 K) compared to diamond's, render the magneto-optical properties of defect qubits highly temperature-sensitive.

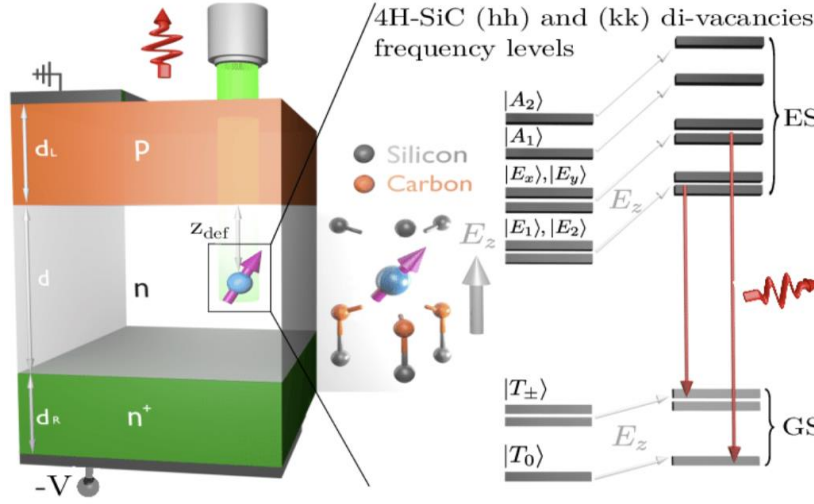


Fig. 2.5 Schematic view of the 4H-SiC p-n-n + diode with one divacancy located in the n region at $z = z_{\text{def}}$. The (hh) or (kk) divacancy lattice configuration is shown together with the response of its frequency to an applied electric field (E_z along the defect symmetry axis) produced by the diode voltage. The red arrows represent the PL transitions³¹.

2.3 Defect Centers Hosted in 2D Materials:

2D materials exhibit reduced dimensionality and weak screening effects³², leading to unique physical properties such as linear electron dispersion relation in graphene and strong excitonic effects in atomically thin TMDs flakes. Recent years have seen a proliferation in 2D materials research due to their distinctive physical properties for quantum information science³³. The capability to create and precisely position quantum defects using contemporary experimental techniques represents a significant advantage of 2D vdW materials. These materials offer promising avenues for quantum scaling by leveraging features such as vdW interlayer coupling and inert surfaces that lack unsaturated dangling bonds. These characteristics help overcome challenges faced by bulk materials, such as magnetic noise in spin defects and spectral diffusion in color centers.

Controllable Defect Positions: Current experimental techniques allow for precise control over defect creation in 2D materials, enabling nearly deterministic defect locations essential for scaling qubits. Also, strain, electric and magnetic fields can be intentionally engineered, and optical cavities can be constructed to satisfy required quantum properties. The single-layer MoS₂ layers, delta-doped diamond slabs, and Si thin slabs were predicted as promising hosts for spin qubits. Also, electrons are injected from the metallic tip into the discrete defect states of two-dimensional materials, selectively exciting individual defects without being affected by the luminescence of the bulk crystal background.

Stacking: 2D materials offer substantial flexibility in forming heterostructures with rotational or translational variants, leading to novel electronic and optoelectronic phenomena. The layer-dependent electronic structures and flat band correlations enhanced by different interlayer couplings provide opportunities for incorporating quantum bits, such as sandwiching an atom or molecule between layers. For instance, h-BN with an AA' stacking order functions as a wide-bandgap semiconductor suitable for deep ultraviolet emitters, photodetectors, and photon devices with strong single-photon emission. It also serves as an insulator in gate dielectrics, passivation layers, and atomic tunneling layers, with superior thermodynamic stability compared to other polymorphs.

Surface Properties: Beyond quantum computing and communication, 2D materials inherently serve as excellent platforms for quantum sensing due to their surface properties. The embedding of SPEs in monolayers circumvents issues like total internal reflection common in 3D color centers, significantly improving light extraction efficiency.

Isotopic Purity: Isotopic purification in 2D materials significantly extends spin coherence times, with records reaching up to 30 ms [Ye, M.; Seo, H.; Galli, G. Spin Coherence in Two-Dimensional

Materials]. Compared to 3D materials, 2D vdW materials excel in controllable generation and manipulation of properties.

2.3.1 Hexagonal Boron Nitride

Boron nitride (BN) crystallizes in three primary forms: cubic boron nitride (c-BN), wurtzite boron nitride (w-BN), and hexagonal boron nitride (h-BN). Among these, c-BN, with its tetrahedral sphalerite lattice structure, is one of the hardest known materials, exhibiting high thermal conductivity, hardness, and chemical inertness. w-BN represents another sp^3 hybridized phase of BN, consisting of alternating tightly packed boron and nitrogen layers. In contrast, h-BN is composed of boron and nitrogen atoms arranged in an sp^2 hybridized honeycomb lattice structure, isomorphic with graphene. Each adjacent layer in h-BN is formed from highly polarized B-N covalent bonds and held together by weak van der Waals forces. The bond length within h-BN is 0.145 nm, with an interlayer distance of 0.334 nm. Unlike graphene or monoelemental graphite, h-BN is strongly polarized due to the electronegativity difference between its constituent atoms, leading to in-plane anisotropic properties and unique electronic and optical characteristics dependent on the stacking order. h-BN is a wide bandgap (~6 eV) 2D material that can host color centers, making it a promising candidate for quantum technology applications. Many emitters in defective h-BN exhibit bright emissions with narrow linewidths, tunability, and high stability. The origins and characteristics of single photon emissions (SPEs) in defective h-BN have been explored using resonant inelastic X-ray scattering (RIXS) techniques, identifying a range of fundamental energies covering a broad spectrum from mid-infrared to ultraviolet, which correlates with photoluminescence (PL) spectra observed within the visible range.

Various defects can serve as potential candidates for quantum applications hosted in h-BN³⁴, as summarized in Fig. 2. Theoretical studies and experimental observations have identified plausible

as well as more complex clusters, are illustrated. In simplified notation, $C_B C_N$ and $V_B V_N$ for triple defects are abbreviated as CC and VV, respectively. The C60 and C6H denote carbon clusters arranged in a ring and 'H' shape, respectively³⁴.

The following discussion discusses typical defects from single-site to quadruple-site. Since the observation of SPEs at room temperature in 2015³⁵, specific quantum emitters in h-BN remain elusive, with their origins still actively investigated. Studies conducted by Ondrej L. Krivanek et al. using scanning transmission electron microscopy (STEM) have shown that substitutional impurity defects such as O_N , C_N , and C_B frequently form pairs. The zero-phonon lines at 4.1 and 5.3 eV were tentatively assigned to deep donor C_B and deep acceptor C_N , respectively, based on DFT simulations. Abdi et al. theoretically posited that the negatively charged boron vacancy (V_B^-) exhibits a spin triplet ground state, making it suitable for scalable qubit systems and SPEs. The V_B^- center in h-BN, with D_{3h} point group symmetry, demonstrates robust photoluminescence emission at $\lambda_{\max} = 800$ nm at room temperature. Its electronic structure mirrors that of the diamond NV center, featuring a triplet ground state (3A2) and a ZFS of approximately 3.47 GHz between the spin sublevels $m_s = 0$ and $m_s = 1$. These theoretical predictions have received experimental validation through optically detected magnetic resonance (ODMR) and electron paramagnetic resonance (EPR) measurements conducted by Gottscholl et al. in 2020.

The $V_N N_B$ defect (a nitrogen vacancy adjacent to a boron-substituted carbon) can produce a spin triplet ($S = 1$) ground state in h-BN³⁶, suggesting its potential for hosting defect qubits. In contrast, Sajid and co-workers identified the ground state of $C_N V_B$ as a 1A1 singlet with C_{2v} symmetry, predicting a 2.08 eV zero-phonon line (ZPL) energy for its emission with a likely broad phonon sideband. Additionally, the neutral carbon trimer defects $C_2 C_N$ and $C_2 C_B$ are proposed to have ZPL energies of 1.62 and 1.65 eV, respectively, with a phonon sideband of approximately 160 meV,

potentially explaining the 1.95 eV emitters observed in h-BN [T. Tran, K. Bray]. McDougall et al. utilized X-ray absorption near-edge structures (XANES) and density functional theory (DFT) calculations to explore the shifts in core levels of host atoms, identifying the presence of O_N and V_B3H defects — the latter being a boron vacancy quenched by three hydrogen atoms. As h-BN samples exhibited a 4.1 eV emission, this was tentatively assigned to the V_B3H defect, despite DFT calculations underestimating the bandgap by about 1.5 eV.

Regarding carbon trimer and tetramer defects, Jara et al. indicated that the neutral C_2C_N and C_2C_B defects might have ZPL energies of 1.62 and 1.65 eV, respectively, accompanied by a phonon sideband of around 160 meV. Omid Golami et al. conducted an enlightening analysis using a combination of ab initio methods and group theory, revealing several radiative transitions along with spin-orbit and spin-spin assisted nonradiative transitions. Furthermore, spin-spin interactions result in a splitting between quartet states $4A_2$. Benedek et al. employed complementary first-principles methods to study neutral nitrogen and boron site-centered symmetric carbon tetramers in hBN, predicting their electronic, optical, and spin properties. Their findings indicated that symmetric carbon tetramers possess a high-spin ground state, visible-range optical transitions, singlet shelving states, and strain-dependent non-radiative decay channels. It was concluded that C_4N and C_4B defects are viable for spin qubits and sensing applications. Moreover, it was shown that strain could be utilized to tailor the spin contrast of these defects, potentially expanding the applicability of spin qubits in hBN.

N-poor conditions					N-rich conditions				
Defect	Max.density	Symmetry	Spin	E_{ZPL}	Defect	Max.density	Symmetry	Spin	E_{ZPL}
C_N	2×10^{17}	D_{3h}	1/2	2.5	C_B	1×10^{18}	D_{3h}	1/2	1.7

N-poor conditions					N-rich conditions				
C_2	3×10^{16}	C_{2v}	0	4.1	C_2	3×10^{16}	C_{2v}	0	4.1
C_2C_N	2×10^{15}	C_{2v}	1/2	1.6	C_2C_B	1×10^{16}	C_{2v}	1/2	1.7, 1.4
C_B^+	3×10^{14}	D_{3h}	0	\	$C_N(C_B)_3$	5×10^{14}	D_{3h}	1	≈ 2.0
$C_B(C_N)_3$	3×10^{13}	D_{3h}	1	≈ 2.2	C_N^-	1×10^{14}	D_{3h}	0	\
C_4	3×10^{13}	C_s	0	3.1	C_4	3×10^{13}	C_s	0	3.1
				(trans),					(trans),
				3.5 (cis)					3.5 (cis)

Tab. 2.2 Summay about the carbon-related defects with the maximum equilibrium densities measured in cm^{-3} , under growth conditions at a temperature of $T = 1600$ K with no oxygen present during the growth phase. The ZPL energies, denoted as E_{ZPL} , for internal defect transitions are expressed in eV. These E_{ZPL} values are sourced from previously published theoretical studies, calculations presented in this paper, or approximations as discussed in the text, with the latter indicated by the symbol “ \approx ” preceding the value. All energy values are rounded to within 0.1eV. Unless explicitly indicated, the defects are considered to be charge neutral.³⁷

2.3.2 Transition metal dichalcogenides

Transition metal dichalcogenides (TMDs) are typical semiconductors with bandgaps ranging from the near-infrared (NIR) to visible (VIS) light spectrum. This property renders them ideal for applications in optoelectronic devices, including photodetectors, solar cells, and biosensors³⁸. The crystalline structure of 2H-TMDs is characterized by the P63/mmc space group and consists of stacked $X - M - X$ layers. In these layers, a metal plane ($M = \text{Mo}, \text{W}$) is flanked by two trigonal planes of chalcogen atoms ($X = \text{S}, \text{Se}, \text{Te}$). Interlayer bonding in TMDs is governed by weak van der Waals forces, while strong covalent bonds maintain the integrity within the $X - M - X$ layers. Such configuration enables

the exfoliation of TMDs into single and few-layer structures via mechanical and chemical methods, which significantly alters their physical properties.

Monolayer TMDs, such as WS_2 and MoS_2 , distinctly exhibit a direct bandgap at the K point of the Brillouin zone, unlike their multilayer counterparts which show an indirect bandgap. Additionally, monolayer TMDs feature pronounced spin-orbit coupling, leading to considerable spin splitting in the valence and conduction bands, which are on the order of several hundreds and tens of millielectronvolts, respectively. Unique to monolayer TMDs is the time-reversal symmetry alongside broken inversion symmetry, which manifests as non-equivalent valleys in momentum space with opposite pseudospins, identified as $|K\rangle$ and $|K'\rangle$. These properties produce novel physical phenomena, including chirality-dependent optical selection rules, spin-valley locking, and the valley Hall effect. Such characteristics provide a robust physical basis for quantum computing using valley pseudospin qubits in TMDs³⁹.

Unlike h-BN discussed in section **2.3.1**, the exploration of optically addressable spin defects in TMDs are largely grounded in theoretical exploration rather than empirical studies. This field has garnered interest since SPEs are discovered in TMDs in 2015⁴⁰. These studies revealed PL emissions from monolayer WSe_2 at cryogenic temperatures, with energies 20-100 meV lower than those of intrinsic excitonic emissions. These emissions are characterized by photon antibunching, narrow linewidths as low as 0.1 meV, linear polarization, and lifetimes on the order of 1 ns. The associated neutral localized excitons often manifest a fine-structure split doublet, distinguished by orthogonal linear polarizations and a splitting ranging from 0.4 to 0.8 meV, typically related to either electron-hole exchange interactions or strong Coulomb forces.

Further research has identified similar SPEs in other TMDs such as MoS₂, WS₂, and MoSe₂. The origin of SPEs in these materials is debated, with two primary types identified: The first type resembles a color center, similar to an isolated artificial atom with electronic states deeply embedded within the bandgap, typically influenced by local strain effects over scales significantly exceeding the exciton Bohr radius of TMDs. Although local deformations may localize excitons on scales as small as 10 nm, the genesis of SPEs likely involves a combination of strain, disorder, and defects. The second type, referred to as a quantum dot (QD), features emissions from bound excitons within a potential well created by local strain. SPEs have been successfully produced in MoS₂ by encapsulating monolayers between two h-BN layers post-irradiation, enhancing excited state lifetimes and promoting clear antibunching.

TMDs have been proven potential platforms for multi-qubit operations. In isotopically purified MoS₂ layers, the spin coherence time could extend up to 30ms⁴¹. Tsai et al. proposed a model integrating symmetry constraints and electronic structure of the host material to screen for defect spin qubits with inherently stable triplet ground states. Their comprehensive search identified thermodynamically stable neutral anion-anti-site defects across six monolayer 1H-TMD compounds^{42,43}. The Fermi level in these defects exhibits energy windows at 1.43eV, 0.88eV, 0.48eV, 1.01eV, 1.24eV, and 0.19eV for W_S^0 , W_{Se}^0 , W_{Te}^0 , Mo_S^0 , Mo_{Se}^0 , and Mo_{Te}^0 . The defect levels of W_S^0 and W_{Se}^0 were selected as the most favorable for qubit realization. Specifically, the electronic configuration of W_S^0 includes a triplet ground state 3A_2 and a triplet excited state 3E , mirroring the defect levels found in the NV center of diamond. The zero-phonon ZPL for the transition between these states is 0.727eV (1.7 μ m) in NIR range. Furthermore, the positions of singlet states 1E and 1A_1 , are determined with the consideration of Coulomb interactions to identify nonradiative decay paths that bridge the triplet and singlet state. As presented in Fig. 6e, the energy difference between 1E and 3A_2 for W_S^0 is 0.151eV, with a computed ZFS of 7.89GHz—

significantly higher than the 2.88GHz in diamond's N_V center. The identification of three permissible intersystem-crossing paths Γ_0^\perp , Γ_1^\perp , and Γ_2^Z was achieved by analyzing the spin quantum numbers and irreducible representations (IRs) of tensor products of wavefunctions and spinors. As shown in Fig. 2.7f, the initialization, manipulation, and readout of TMD-based anti-site qubits are analogous to working mechanisms in diamond hosted defects.

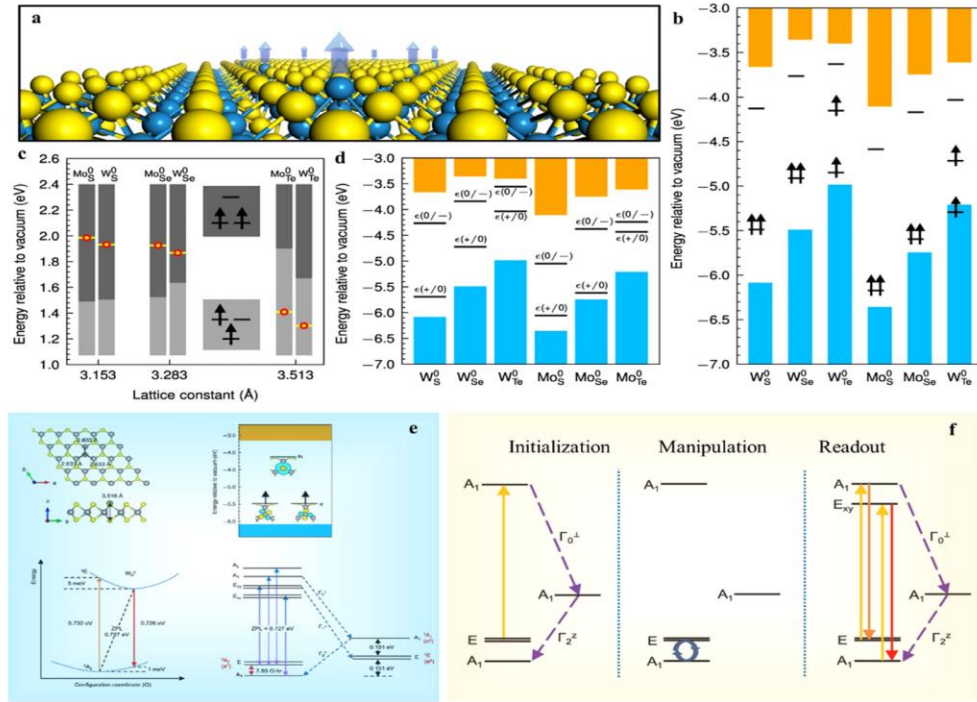


Fig. 2.7 Anion-antisite defect qubits in six 1H-TMDs. (a) Geometry of the M_x^0 antisite point defect in single-layer 1H-TMD. (b) Defect levels of M_x^0 in band gaps of 1H-TMDs with ground-state triplets. (c) The correlation between the level splitting of defect and the relative z-positions of the anion antisites and neighboring cations. (d) Thermodynamic transition energy levels of antisite point defects in six 1H-TMDs. (e) Geometric and electronic properties for the neutral antisite defect W_S^0 in WS_2 . (f) An operational loop based on the antisite qubit W_S^0 ⁴³.

Another promising spin qubit candidate is the carbon defect in WS_2 , specifically a carbon atom substituting for a sulfur atom (C_s), as depicted in Fig. 2.7. Utilizing scanning tunnelling microscopy (STM) tips, precise and on-demand atomic modifications are feasible. Through DFT HSE calculations, Li et al. elucidated the electronic structure and optical properties of C_s , affirming its viability as a qubit. The spin of C_s can be optically initialized and read out, with a coherent state achievable via microwave excitation. As illustrated in Fig. 2.7, the fundamental state is a closed-shell singlet 1A_1 , and a spin-conserving optical transition to the excited state 1E is marked by a ZPL of 0.923eV (approximately 1340nm). Following excitation to 1E , a highly selective intersystem crossing (ISC) to the $m_s = 0$ state of triplet 3E occurs, with its fine structure shaped by complex interactions among phonons, orbitals, and spins. The ISC process is notably rapid, with a lifetime in the picosecond range, considerably shorter than the radiative lifetime of the 1E state. Optical pumping can initialize the $E_{x,y}$ state, effectively setting a quantum level. The optical lifetime of 3E extends to 145ns, with a calculated radiative rate of $1.10(2\pi)\text{MHz}$ in angular frequency. Fig. 7d illustrates the procedure for optical initialization and readout of the electron spin qubit state. The coherence time for the $S = 1$ qubit in WS_2 is approximately 11ms, predominantly due to substantial hyperfine interactions between the electron and nuclear spins near the defect. Additionally, the presence of ^{13}C , with its significant hyperfine interaction, should be avoided in ancillary qubit roles to prevent decoherence.

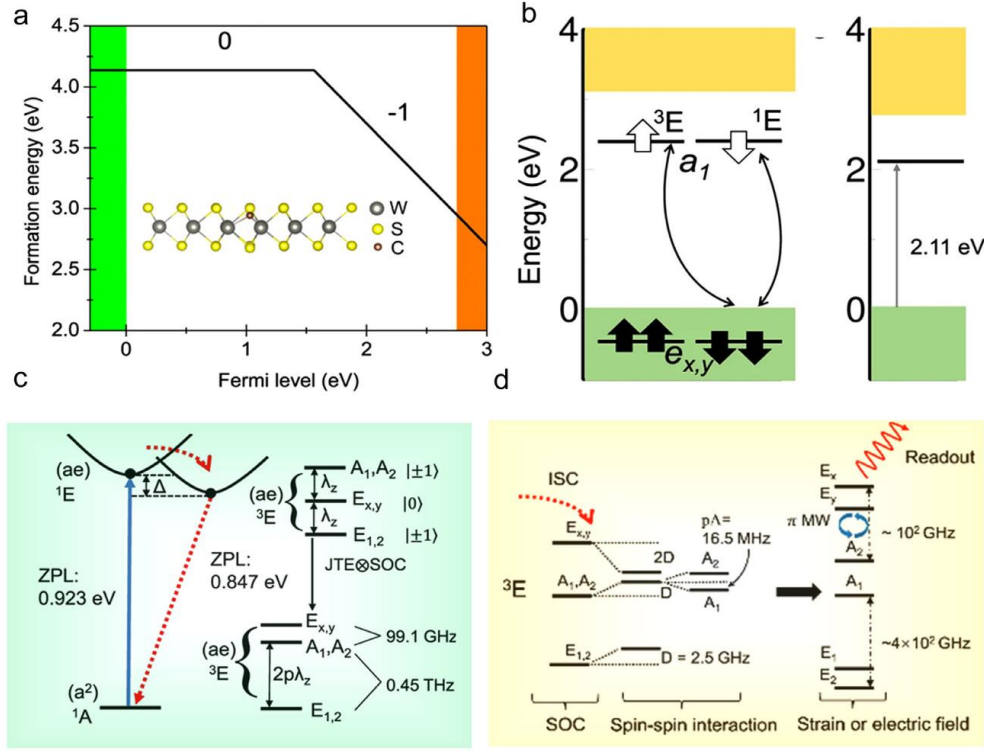


Fig. 2.8 Carbon defect qubit in WS₂. (a) Formation energy as a function of Fermi-level for C_S defect. The energy diagram without SOC effect (b) and with SOC effect (c) for neutral C_S defect at ground state. (d) The possible optical transition among ground state and excited states of C_S⁰⁴².

2.4 Other Potential Host Materials

2.4.1 Zinc Oxide

Point defects in ZnO have garnered attention as potential single-photon sources⁴⁴, motivated by numerous studies examining its electrical and optical properties alongside a bandgap of approximately 3.4 eV. Defects such as oxygen vacancies (V_O), zinc vacancies (V_{Zn}), zinc interstitials (Zn_i), and oxygen interstitials (O_i) play significant roles in these properties [A. Janotti 2009]. Hybrid density functional calculations have provided insights into native vacancies, interstitials, and dangling

bonds within ZnO. Notably, the oxygen vacancy V_O , characterized as a neutral defect, exhibits its highest-energy photoluminescence peak at 0.62eV.

Under typical growth conditions, the zinc vacancy (V_{Zn}) emerges as the lowest-energy native defect in n-type ZnO, functioning as an acceptor and yielding multiple transition levels with emissions ranging from 1 to 2eV. The presence of hydrogen atoms forms stable complexes with $V * Zn$, altering the acceptor levels towards the valence band edge. These hydrogenated V_{Zn} defects exhibit optical transitions akin to those of the isolated V_{Zn} , aligning well with recent experimental findings and supporting their role in photon emission. Additionally, Zn dangling bond-related emissions are proposed as an intrinsic source of green luminescence in ZnO.

Room temperature quantum emitters with broad phonon sidebands have been linked to various charge states of the Zn-vacancy. Moreover, room temperature single-photon emissions were observed in ZnO nanoparticles. The advancement of quantum technologies using ZnO hinges on a deeper understanding of these optical characteristics. The interaction between Znd orbitals and Op orbitals complicates accurate DFT calculations of both pristine and defective ZnO compared to other semiconductor materials. Although hybrid DFT functionals have significantly advanced this field, ongoing efforts are necessary to further elucidate the localized and correlated orbitals of these vacancies and related defects.

2.4.2 Gallium Nitride

Room temperature quantum emitters in gallium nitride (GaN) have been recognized for their narrowband luminescence properties². In typical semiconductor quantum dots, high densities of defects and charge traps often lead to rapid charge fluctuations, which can substantially broaden the emission linewidth. To mitigate this, interface fluctuation GaN quantum dots were introduced, utilizing

charge localization centers that form at thickness variations within quantum wells. These specialized quantum dots emit in the near ultraviolet spectrum and maintain narrower linewidths compared to conventional quantum dots. Recent developments in GaN technology have also uncovered near-infrared emitters, notable for their exceptional photon purity and unprecedented brightness, surpassing 10^6 counts/s. Despite these advances, the precise origin of these emitters remains elusive. Among the promising candidates for qubit applications within GaN, the substitutional chromium (Cr^{4+}) impurity has been identified. This impurity features minimal phonon sidebands, enabling a higher fraction of fluorescence to be effectively utilized in quantum communication processes .

2.4.3 Real-earth Materials

Rare-earth ions (REIs) embedded in solid-state matrices are considered potential components for quantum memory and quantum communication applications⁴⁵. Notably, europium-doped Y_2SiO_5 or YSO has demonstrated the capability to store quantum information for up to six hours. In these REI systems, the $4f$ electrons experience splitting in the low symmetry crystal field, giving rise to optical transitions originating from these split atomic states. These atomic-like states afford narrow optical emission lines due to the sizable hyperfine structure in the ground state, facilitating long coherence times. However, a drawback is the long optical lifetimes, as the transitions between these atomic states are often first-order forbidden.

This limitation has been partially overcome in Pr^{3+} -doped $\text{Y}_3\text{Al}_5\text{O}_{12}$ or YAG through an upconversion process. This process benefits from accessing short-lived excited states and providing background-free optical imaging, marking the first demonstration of REI quantum emission at helium flow temperatures. Subsequent studies demonstrated quantum emission of Pr^{3+} -doped LaF_3 at 1.5K. In addition, spin-to-photon interface and single spin readout have been achieved in Ce^{3+} -doped YAG,

where the optical transition occurs between the $5d$ excited state and $4f$ ground state. The $4f$ states exhibit significant mixing with orbital momentum, enabling spin-flip optical transitions between $4f$ and $5d$ levels with an optical lifetime of approximately 60ns. Under dynamic decoupling, the spin coherence lifetime extends to $T_2 = 2\text{ms}$, nearly reaching the measured spin-lattice relaxation time of $T_1 = 4.5\text{ms}$.

Another strategy to enhance the intrinsically low emission of REIs involves placing them near high-quality optical resonators to exploit the Purcell effect, which selectively boosts the rate of spontaneous emission. This approach has recently been implemented with Er^{3+} -doped YSO and ytterbium-doped YVO_4 ⁴⁶. By optimizing the orientation of an external constant magnetic field, the enhancement of emission has been tailored specifically toward spin-conserving excitations, enabling distinct optical transitions for different spin states. If the laser and cavity modes are aligned with one of the spin-conserving excitation energies, emission is expected only for the resonant bright spin state, with no emission for the off-resonant dark spin state. During optical cycles, a low-probability spontaneous decay from the bright to the dark state can occur, remaining non-emissive. Thus, detecting emission correlates directly with the spin state of the REI in its ground state.

3 Key Quantities and DFT Approaches

Identifying novel Quantum Point Defects (QPDs) is a combinatorial challenge, with millions of potential host-defect combinations. Besides three basic QPD classes—vacancy, interstitial, and substitution, complex defects can be created by advanced fabrication techniques. The massive parameter space makes exhaustive experimentation impractical. Consequently, the traditional historical approach, starting from a specific structure, becomes unrealistic. Meanwhile, advancements

in quantitative theoretical predictions, especially in Density Functional Theory (DFT), have enabled a new approach. Utilizing DFT calculations, particularly high-throughput methods, selects specific defects from the vast chemical space for targeted applications, followed by experimental verification^{42,47}. This workflow is increasingly adopted. Moreover, computational databases derived from full parameter space searches, like the Quantum point defects in 2D materials - the QPOD database⁴⁸, facilitate establishing relationships as depicted in Fig 3.2 between materials properties, defect properties, and defect functionality, enabling discovery by design. Building a DFT calculated databases and subsequently leveraging modern machine learning techniques to explore connections or make predictions is a popular contemporary research approach^{49,50}.

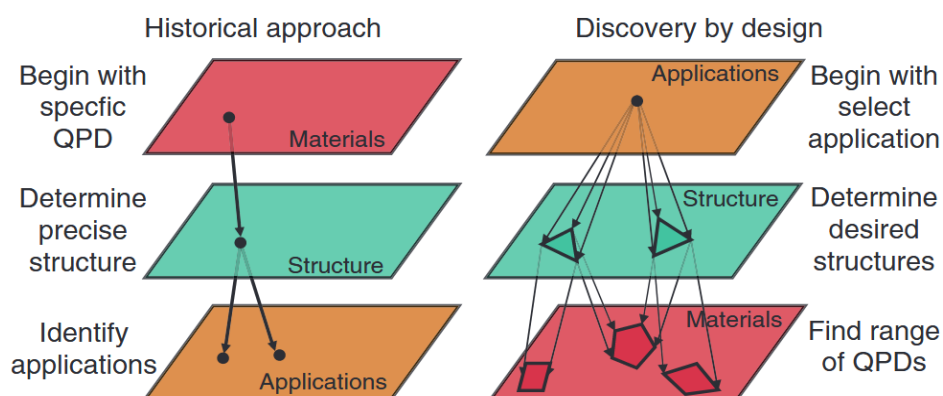


Fig. 3.1 An efficient DFT approach to QPD discovery would possibly convert the traditional paradigm (left) to identify materials and defects optimized for specific applications in quantum science (right)⁴⁹.

Each application demands specific functionalities, closely tied to the defect's structural and functional attributes and its host. These relationships are illustrated in Fig. 3.2, where lines show significant connections for defining QPD properties or functions, and circle sizes reflect the number of connections. This diagram, while not comprehensive, highlights how various features together contribute to distinct quantum functionalities.

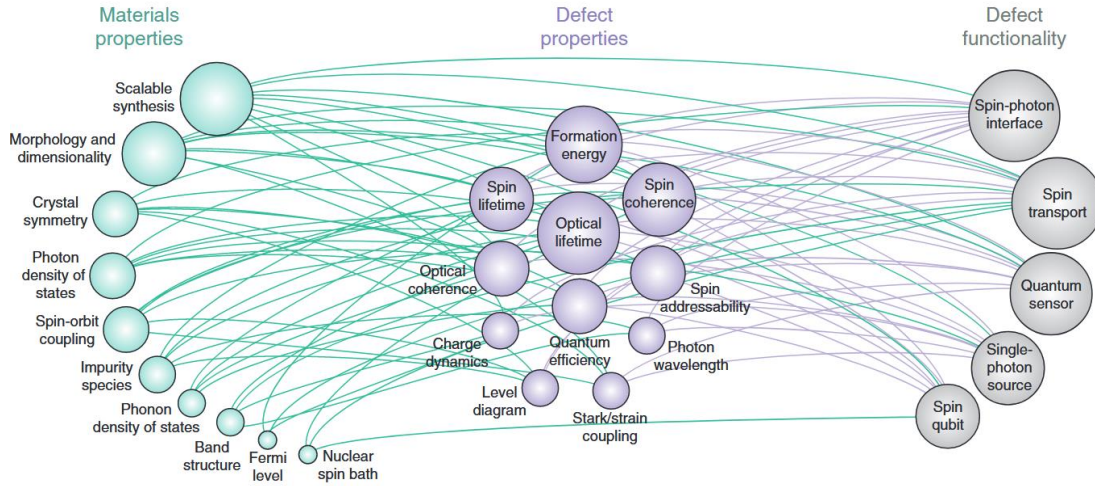


Fig. 3.2 The functionality of a defect for quantum science applications depends in complex ways on the defect's properties, which are in turn related to the fundamental properties of the host material and the defect's composition².

Effective QPD analysis and design should refer to previous methodologies, combining analytical and computational theory to predict how host symmetry, defect configuration, and chemical composition coupling to produce the desired electronic structure for a required application. In the following sections, selected key quantities in the evaluation of quantum point defects will be discussed. Under practical DFT considerations, properties of QPDs can be divided into three major categories, as summarized in Table 3 and described in detail:

Basic ground-state properties: The general DFT formalism for calculating ground-state point defects have been well established. Freysoldt et al. provide a comprehensive review on the theoretical framework, practical implementations, and amenable experimental quantities. The formalism is based on formation energies, with all possible charge and spin states being considered. The key calculated quantities include defect formation energies, charge transition levels, and defect geometries in different charge states, ground-state spin configurations, and vibrational properties.

The existing methodology to calculate these properties is satisfying, universally accepted, and its extensive applications push forward many well-integrated code packages such as pydefect⁵¹, DASP⁵², Spinney⁵³ and doped⁵⁴. The current ongoing research endeavor aims at automated operations for high-throughput calculations.

Specific ground-state properties: A variety of related response properties can be derived from the electronic ground state, which can be verified by dedicated experiments and theory. Analysis on such response or dynamical properties are not common in traditional point defect research. Obviously, the spin-related quantities including zero-field splitting, spin-orbit coupling and hyperfine coupling are crucial for QPDs in precisely determining the many body electronic structure. Phonons also heavily influence optical excitation and luminescence. Optical excitation typically leads to a vibronic excited state, with the transition probability proportional to the overlap between the ground state and the vibronic excited state. The vibronic state releases energy by emitting phonons. A similar process occurs during luminescence. Direct transitions between the non-phonon-excited ground and excited states, facilitated by the zero-point motion of local vibrational modes, result in ZPL and absorption lines. Electron–phonon coupling is not a spin-dependent phenomenon, it still can indirectly affect the expectation values of spin-dependent observables.

Excited state properties: The constrained occupation DFT method has been developed to make DFT go beyond ground state, which describes excitation processes in terms of a single Slater determinant of the Kohn–Sham particles. Once the excited state wavefunction is obtained, we can have qualitative understanding of multiplet structure and optical transitions, in particular the polarization of emitted light, transition dipole moments, and radiative lifetimes. In addition, by studying lattice relaxation due to optical excitation, Huang-Rhys factors can be calculated to quantify electron-phonon coupling. photoluminescence line shapes, absorption and photo-ionization cross sections can

also be determined rather straightforwardly. Studies of nonradiative transitions, including carrier capture rates that are important for understanding QPD charge dynamics, are now feasible as well. Apart from difficulties in describing the excited state itself, the subsequent calculation of properties poses practical rather than fundamental problems.

Category	Defect properties	Status of development
Basic ground-state properties	Geometries, defect formation energies, charge-state transition levels, ionization levels, ground-state spin multiplicity, vibrational modes and frequencies	Methodology well-developed and accepted, widely implemented and tested, ready for high-throughput calculations
Specific ground-state properties	Magnetic interactions (zero-field splitting, spin-orbit, hyperfine), electron-phonon coupling, spin-phonon coupling	No principle difficulties, may be practical difficulties, not widely implemented yet, developments and testing taking place
Excited-state properties	Excited-state energies and geometries, multiplet structure, transition dipole moments, radiative rates, optical lineshapes, nonradiative transitions	Principle difficulties persist, rigorous approaches computationally very expensive, need for approximate methods that have to be tested more systematically

Tab. 3.1 Practical QPD property categories and their status of development

3.1 Crystal Symmetry

The Born–Oppenheimer approximation is commonly employed for the electron–nuclei system of point defects, where ions are considered as charged particles possessing atomic masses, and electrons rapidly traverse the adiabatic potential established by these ions. The total energy of electronic states is calculated as a function of the ions' coordinates within the system, enabling the mapping of the

adiabatic potential energy surface (APES). The global energy minimum on the APES for a specified electronic configuration is determined by minimizing the quantum mechanical forces exerted on the ions. Additionally, quasi-harmonic vibration modes are calculated by fitting a parabola around the global minimum, displacing the ions from their equilibrium positions, and solving the Hessian equation. In QPD studied, the symmetry distortions, or Jahn-Teller effect, are commonly observed and investigated. The Jahn-Teller effect posits that a system possessing a spatially degenerate electronic state will undergo spontaneous geometrical distortion, breaking symmetry to reduce the system's overall energy. Abtew et al. examined the dynamic Jahn–Teller effect in the $3E$ excited state of a diamond NV^- center. To elucidate this effect, the APES was derived from constrained DFT calculations. For the NV center, six symmetrized displacements featuring two A_1 and two E vibrations are induced by the motion of atoms neighboring the vacancy. The totally symmetric A_1 vibrational modes do not alter the symmetry, whereas the E vibrational modes reduce the symmetry and split the defect levels. Dephasing of the zero-phonon line (ZPL) in the NV center is predominantly influenced by the interaction between the doubly degenerate E state and the E phonon modes, leading to a T^5 dependence of the ZPL linewidth.

Group theory is the prevailing tool to achieve qualitative – and sometimes quantitative – understanding of defect electronic structure and optical dynamics⁵⁵. According to group theory, the point group determines the multiplicity of each energy level and higher symmetry allows for degenerate orbitals. Degenerate orbital levels are important, since, as per Hund's rule, they will give rise to high spin states ($S > 1/2$) in the electronic ground state. High spin states are often desirable for QPDs, as they exhibit zero-field splitting parameters in the spin Hamiltonian; this decouples the QPD from background electronic impurities in the material with $S = 1/2$ and allows for coherent spin control even at zero magnetic field. Orbital degeneracies also give rise to various spin-orbit combinations

with definite symmetry in the electronic ground or excited state that can produce spin photon entanglement.

The study of crystal field theory can be applied in such situations where it is desirable to exploit the sharp, discrete energy levels that are characteristic of atomic systems together with the larger atomic densities that are typical of solids. As an example, consider the variety of powerful lasers whose operation is based on the population inversion of impurity levels of rare earth ions in a transparent host crystal. The energy levels of an electron moving in the field of an ion embedded in such a solid are approximately the same as for an electron moving in the field of a free ion. Thus the interaction between the ion and the host crystal can be treated in perturbation theory.

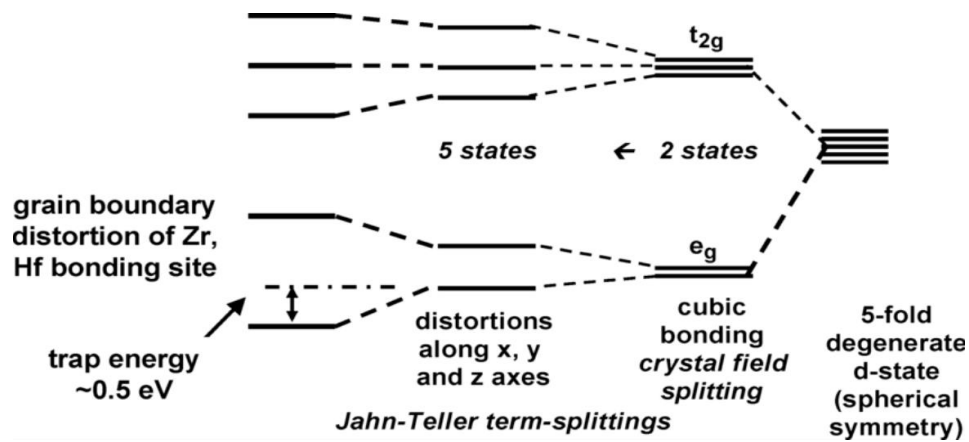


Fig. 3.3 schematic representation of the Jahn–Teller distortions in TM elemental and complex oxides with eight-fold coordination, including the grain-boundary defect states⁵⁵.

All states with an energy in the band gap are classified according to the symmetry group of the defect⁵⁶. In a first step, the point group, G , of the defect is determined. To determine G we first reintroduce the relaxed defect into a supercell that preserves the symmetry of the host material, i.e. map the relaxed atomic positions from the symmetry broken calculation into a simple repetition of the primitive unit cell vectors. The second step is to correctly obtain G as the point group of the

symmetry broken supercell. The high-symmetry supercell is only used to determine G while all actual calculations are performed for the low-symmetry supercell. The defect states in the band gap are labeled according to the irreducible representations (irrep) of G ⁵⁷. The irrep of given eigenstate, $\psi_n(\mathbf{r})$, the matrix elements are given by

$$\Gamma(R) = \Gamma_{nn}(R) = \int d\mathbf{r} \psi_n(\mathbf{r})^* R \psi_n(\mathbf{r}) \quad (3.1)$$

where R is any symmetry transformation of G . It follows from the orthogonality theorem that the vector $\Gamma(R)$ can be expanded in the character vectors, $\chi^{(a)}(R)$,

$$\Gamma(R) = \sum_a c_a \chi^{(a)}(R) \quad (3.2)$$

where the quantity c_a represents the fraction of ψ_n that transforms according to the irrep a . For any well localised defect state, all the c_a will be zero except one, which is the irrep of the state. In general, less localised states will not transform according to an irrep of G . That is because the wave functions are calculated in the symmetry-broken supercell. If the representation is reducible, then crystal field splittings of the energy levels occur.

In practice, we can refer to Symmetry of Rotations and Cartesian products and Symmetry of Spherical Harmonics (multipoles) provided by Gernot Katzer, where the orbital basis functions and splitting details can be checked.

Symmetry of Rotations and Cartesian products

		Rot	Tr=p	-d-	-f-	-g-	-h-	-i-
A_{1g}	g+i 2k+2m							
A_{2g}	i m							
E_g	d+g+i 2k+2m							
T_{1g}	R+g+i 2k+2m							
T_{2g}	d+g+2i 2k+3m							
A_{1u}	i							
A_{2u}	f j+l							
E_u	h j+l							
T_{1u}	p+f+2h 2j+3l							
T_{2u}	f+h 2j+2l							

Symmetry of Spherical Harmonics (multipoles)

Angular momentum	Multipole order	Symmetry	permanent moment?
S ($\ell=0$)	1 (monopole)	A_{1g}	no
P ($\ell=1$)	2 (dipole)	T_{1u}	no
D ($\ell=2$)	4 (quadrupole)	E_g ⊕ T_{2g}	no
F ($\ell=3$)	8 (octupole)	A_{2u} ⊕ T_{1u} ⊕ T_{2u}	no
G ($\ell=4$)	16 (hexadecapole)	A_{1g} ⊕ E_g ⊕ T_{1g} ⊕ T_{2g}	yes
H ($\ell=5$)	32 (dotriacontapole)	E_u ⊕ 2 T_{1u} ⊕ T_{2u}	no
I ($\ell=6$)	64 (tetrahexacontapole)	A_{1g} ⊕ A_{2g} ⊕ E_g ⊕ T_{1g} ⊕ 2 T_{2g}	yes
J ($\ell=7$)	128 (octacosahexapole)	A_{2u} ⊕ E_u ⊕ 2 T_{1u} ⊕ 2 T_{2u}	no
K ($\ell=8$)	256	A_{1g} ⊕ 2 E_g ⊕ 2 T_{1g} ⊕ 2 T_{2g}	yes
L ($\ell=9$)	512	A_{1u} ⊕ A_{2u} ⊕ E_u ⊕ 3 T_{1u} ⊕ 2 T_{2u}	no
M ($\ell=10$)	1024	A_{1g} ⊕ A_{2g} ⊕ 2 E_g ⊕ 2 T_{1g} ⊕ 3 T_{2g}	yes

<http://blog.sciencenet.cn/u/XRC0808087>
[More...](#)

Fig. 3.4 Splitting of atomic orbital energy levels in the Oh crystal field

Since the multiplication relations among the group elements within a subgroup remain the same as in the parent group, the irreducible representations of the parent group and the subgroup are interconnected according to specific rules known as branching rules. As shown in Table X, atomic orbitals or electronic states correspond to the basis functions of the irreducible representations of the group. This is detailed in the correlation table between the irreducible representations of the D_{3h} group and its subgroups. The irreducible representation (IR) of a high symmetry point group becomes a reducible representation of a lower symmetry point group, with the subgroups being defined through distortions along symmetry-adapted coordinates.

	D_{3h}	C_3	C_{3h}	C_{3v}	C_3	C_{2v}	C_2	C_{2h}	C_s
	A'_1	A_1	A'	A_1	A	A_1	A	A'	A'
	$A''_1 \rightarrow D_3$	A_1	A''	A_2	A_2	A_2	A	A''	A''
	$A'_2 \rightarrow C_{3h}$	A_2	A'	A_2	A_2	B_1	B	A'	A''
	$A''_2 \rightarrow C_{3v}$	A_2	A''	A_1	A_1	B_2	B	A''	A'
	$E' \rightarrow C_{2v}$	E	E'	E	E	$A_1 + B_1$	$A + B$	$2A'$	$A' + A''$
	$E'' \rightarrow C_{2s}$	E	E''	E	E	$A_2 + B_2$	$A + B$	$2A''$	$A'' + A''$

Tab. 3.1 The correlation of D_{3h} with its subgroups

3.2 Formation Energy and Charge Transition Level

The formalism, or grand canonical approach, is based on formation energies⁵⁸. It enables the analysis of defect and impurity structures and concentrations in crystalline solids. In the case of semiconductors and insulators, it allows the calculation of the relative stability of the different charge states of a given defect, and hence the thermodynamic and optical transition levels associated with deep and shallow centers. This approach is applicable across various crystalline materials, though its relevance may vary among different material classes. Additionally, the formalism accounts for finite-temperature effects, including the computation of free energies that extend beyond configurational entropy.

For a general defect X in the charge state q , the formation energy $E_f[X^q]$ is given by

$$E_f[X^q] = \{E_{\text{tot}}[X^q] - E_{\text{tot}}[\text{bulk}]\} - \sum_i n_i \mu_i + qE_F + E_{\text{corr}} \quad (3.3)$$

where $E_{\text{tot}}[X^q]$ is the total energy of a supercell containing the defect in charge state q and $E_{\text{tot}}[\text{bulk}]$ is the total energy of the defect-free supercell. The chemical potential terms (μ_i) account for the species either added ($n_i > 0$) or removed ($n_i < 0$) from the supercell to create the defect. These terms represent the chemical reservoirs with which atomic species are exchanged, and bounds for these chemical potentials can be set on the basis of the energy of the pure bulk phases of the species or mixed secondary phases. The term proportional to E_F accounts for the electrons added (for $q < 0$) or removed (for $q > 0$) from the defect supercell. The energy of the reservoir for electron exchange is the electron chemical potential or Fermi level (E_F), which is conventionally referenced to

the valence-band maximum (VBM). The final term E_{corr} is a correction term that accounts for finite-size effects that arise due to the use of the supercell technique and can be due to finite k -point meshes, elastic interactions, electrostatic interactions, etc.

$$\Delta H_{D,q}(E_F, \mu) = [E_{D,q} - E_H] + \sum_i n_i \mu_i + qE_F + E_{\text{corr}}$$

Fig. 3.5 illustration of the terms required to compute the charged defect formation energy as function of the atomic and electronic chemical potentials.

Now, as charge correction term will be discussed in the next section, the three terms of the equation and their computation methods in DFT will be discussed in turn⁵⁹.

Term 1: Raw defect formation energy

To obtain ΔE , the standard operating procedure is as follows:

- Fully optimise the crystal structure of the host material in its primitive unit cell.
- Create a supercell expansion that is as close to cubic as possible, which minimises anisotropy in defect-defect interactions.
- The total energy of the pristine supercell becomes the E_H reference for defect formation energies.
- Introduce a defect of your choosing and optimise the structure under constant volume conditions keeping the lattice vectors fixed.
- The total energy of the optimised defective supercell is $E_{D,q}$.

(f) The raw defect formation energy in equation 3 is the difference of two total energy calculations, $\Delta E = E_{D,q} - E_H$.

Term 2: Atomic chemical potentials

The chemical potentials μ_i account for the exchange of species with their environment. Generally, we treat μ_i as a parameter than can vary over the accessible phase space of the material. The standard operating procedure⁶⁰ is as follows:

- (a) Calculate the total energy of the standard states of each element found in host material (e.g. Zn metal and oxygen gas for ZnO).
- (b) Calculate the total energy of all possible secondary phases that could form (e.g. ZnO and Al₂O₃ for a ZnAl₂O₄ host).
- (c) Solve the accessible chemical potential region considering these boundaries. Any point in this stability field can be used safely in equation.

Term 3: Fermi level

The Fermi energy is defined implicitly in DFT calculations, by requiring that the total of the band occupancies f is the number of electrons, N :

$$\sum_{b=0}^{N_b} f_b = N \quad (3.4)$$

where N_b is the number of bands in the calculation. The occupancy is computed from

$$f_b = f \left(\frac{\epsilon_b - E_F}{\sigma} \right) \quad (3.5)$$

where f is the smearing function (e.g. Gaussian, Fermi-Dirac, Methfessel-Paxton), σ is the smearing width, ϵ_b is the band eigenvalue, and E_F is the Fermi energy.

In supercell approach, the charged system with finite size supercell technique suffers from artificial electrostatic interaction between the periodic defect images and background charge. Therefore, correction scheme is needed to remove this interaction from both the total energy calculation and Kohn-Sham (KS) defect levels.

Several different strategies for 2D defect charge corrections have been proposed, mainly falling into two categories: One approach is to derive analytical expressions for the electrostatic energies of point charges in a 2D dielectric medium as a function of supercell size, then the correct limit can be obtained by supercell extrapolation based on these expressions. The other approach is to use the model charge electrostatic self-energy difference between isolated and periodic boundary conditions to approximate the spurious interactions introduced by an extra electron or hole, and then remove the self-energy difference between the two boundary conditions from the defect formation energy.

The most popular approach currently is Freysoldt-Neugebauer-Van der Walle (FNV) correction⁶¹. For two-dimensional systems, the approach described above is complicated by the extreme anisotropy of the system, and in particular by the very weak screening occurring between periodically repeated layers. This means that the electrostatic interaction between a localised charge state and its images in neighbouring cells is generally strong, and the corresponding correction is large.

In GPAW DFT package⁶², FNV method for 2d system is realized as follows: The core of the correction scheme is to write the formation energy of the infinitely dilute system as

$$E^f[X^q]_{\infty} = E^f[X^q]_{\text{supercell}} + E_{\text{correction}} \quad (3.6)$$

results. Because of these difficulties, finding a robust correction scheme in 2D is that much more necessary. The starting point is the same as before, and we write:

$$E[X^q] - E_0 = (E[X^q] - E_0)_{\text{uncorrected}} - E_1 + q\Delta V \quad (3.7)$$

The main problem arises in the E_1 term, and in particular, in finding an appropriate expression for the screened Coulomb interaction of the system. distribution in the same dielectric environment. The first step in calculating either of these is to model the dielectric function. distribution of the system so that we can write

$$\varepsilon_i(z) = k_i \cdot n(z) + 1 \quad (3.8)$$

Where i varies over "in-plane" and "out-of-plane", and n is the in-plane averaged density of the system. The normalization constants, k_i , are chosen such that

$$\begin{aligned} \frac{1}{L} \int dz \varepsilon_{\parallel}(z) &= \varepsilon_{\parallel}^{\text{DFT}} \\ \frac{1}{L} \int dz \varepsilon_{\perp}^{-1}(z) &= (\varepsilon_{\perp}^{\text{DFT}})^{-1} \end{aligned} \quad (3.9)$$

amount of vacuum as the supercell calculation. For 15Å of vacuum, we calculate $\varepsilon_{\parallel}^{\text{DFT}} = 1.80$ and $\varepsilon_{\perp}^{\text{DFT}} = 1.14$. In practice, The FNV corrected formation energy demonstrates excellent agreement with the extrapolated value at infinite supercell size, as shown in Fig. 2.6.

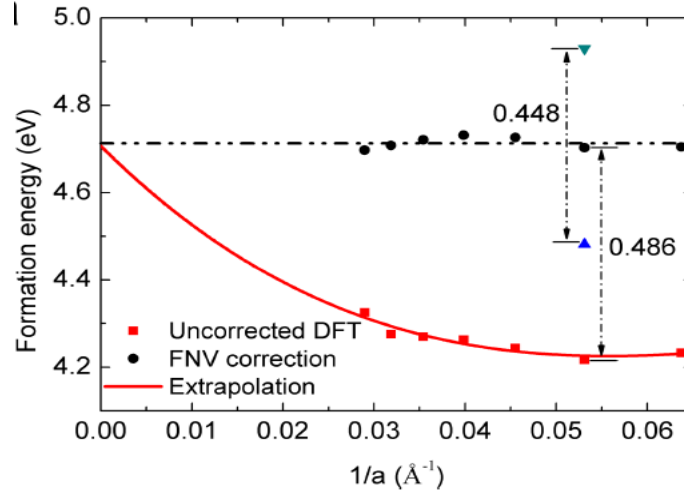


Fig. 2.6 Red square indicates the uncorrected formation energy with different supercell sized of DFT PBE result. The fitted curve is shown by red line and extrapolated to infinite size. Black dot indicates the FNV corrected PBE formation energy and the black dash line represents the averaged FNV formation energy⁴².

3.3 Zero Field Splitting

Zero field splitting is the spin sublevels of the point defect qubits may split even at zero magnetic field. There are two major contributions to the ZFS: the spin-spin and the spin-orbit dipole interactions. The ZFS attributed to SOC is inherently related to the magnetic anisotropy energy of the defect.⁶³ The value of D^{SO} and E^{SO} can be directly calculated by DFT using the expressions:

$$\begin{aligned} D^{SO} &= 2E_{tot}^{DFT}(zz) - [E_{tot}^{DFT}(xx) + E_{tot}^{DFT}(yy)], \\ E^{SO} &= E_{tot}^{DFT}(xx) - E_{tot}^{DFT}(yy). \end{aligned} \quad (3.10)$$

x, y , and z are defined here to be mutually orthogonal electron spin directions assigned in the DFT calculations, according to the convention that $E_{tot}^{DFT}(zz)$ has the largest difference from $E_{tot}^{DFT}(xx)$ and $E_{tot}^{DFT}(yy)$. The z direction is then the spin quantization axis that originates from SOC interactions in the system. As illustrated in Fig. 3a, if the magnetization prefers to align along the spin quantization axis (i.e.,

$D^{SO} < 0, m_s = \pm 1$ is more stable), it can be referred to as easy-axis magnetization; in contrast, easy-plane anisotropy describes the case when the magnetization aligns within a plane perpendicular to the spin quantization axis ($D^{SO} > 0$).

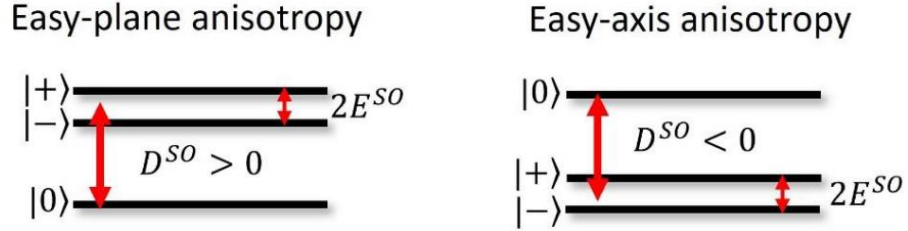


Fig. 3.6 Spin sublevel diagram for easy-plane and easy-axis anisotropy.

The second-order SOC-contributed ZFS has the spin Hamiltonian of

$$\hat{H}_{ZFS} = D^{SO} \left(\hat{S}_z^2 - \frac{1}{3} S(S+1) \right) + E^{SO} (\hat{S}_x^2 - \hat{S}_y^2) = \hat{D}^{SO} + \hat{E}^{SO}, \quad (3.11)$$

which yields, for $S = 1$, $\frac{1}{3}D^{SO} + E^{SO}$, $\frac{1}{3}D^{SO} - E^{SO}$, and $-\frac{2}{3}D^{SO}$ for $|+\rangle$, $|-\rangle$ and $|0\rangle$ eigenstates, respectively (see main text).

For a single spin, with the spin-quantization axis in the z -direction, and spin states $|z\rangle \equiv |\uparrow\rangle$ and $|-z\rangle \equiv |\downarrow\rangle$, we have

$$\begin{aligned} |x\rangle &= \frac{1}{\sqrt{2}} (|\uparrow\rangle + |\downarrow\rangle), \\ |y\rangle &= \frac{1}{\sqrt{2}} (|\uparrow\rangle + i|\downarrow\rangle). \end{aligned} \quad (3.12)$$

Thus, for two spins in the $S = 1$ system,

$$\begin{aligned}
|xx\rangle &= |x\rangle \otimes |x\rangle = \frac{1}{2}(|\uparrow\uparrow\rangle + |\downarrow\downarrow\rangle) + \frac{1}{2}(|\uparrow\downarrow\rangle + |\downarrow\uparrow\rangle), \\
|yy\rangle &= |y\rangle \otimes |y\rangle = \frac{1}{2}(|\uparrow\uparrow\rangle - |\downarrow\downarrow\rangle) + \frac{1}{2}i(|\uparrow\downarrow\rangle + |\downarrow\uparrow\rangle).
\end{aligned} \tag{3.13}$$

Therefore, using the Hamiltonian $\hat{H}_{ZFS} + \hat{H}_{elec}$, the total energies are:

$$\begin{aligned}
E_{tot,xx}^{DET} &= -\frac{1}{6}D^{SO} + \frac{1}{2}E^{SO} + E_{el}, \\
E_{tot,yy}^{DFT} &= -\frac{1}{6}D^{SO} - \frac{1}{2}E^{SO} + E_{el}, \tag{3.14} \\
E_{tot,zz}^{DFT} &= \frac{1}{3}D^{SO} + E_{el}
\end{aligned}$$

where E_{el} is introduced as the total electronic energy, which we assume to be independent of the orientation of the spins. Now, the value of D^{SO} and E^{SO} can be directly calculated by DFT through:

$$\begin{aligned}
D^{SO} &= 2E_{tot,zz}^{DFT} - [E_{tot,xx}^{DFT} + E_{tot,yy}^{DFT}], \\
E^{SO} &= E_{tot,xx}^{DFT} - E_{tot,yy}^{DFT}.
\end{aligned} \tag{3.15}$$

For the calculation of total energies, we first carry out a self-consistent collinear calculation without SOC. Reading from the ground-state charge density of the system, the SOC can be treated as a perturbation in non-self-consistent calculations. The total energy of the system is self-consistently calculated including SOC with a convergence threshold of 10^{-9} eV for different spin orientations.

4 First-principles studies of quantum defects in 2D WS₂

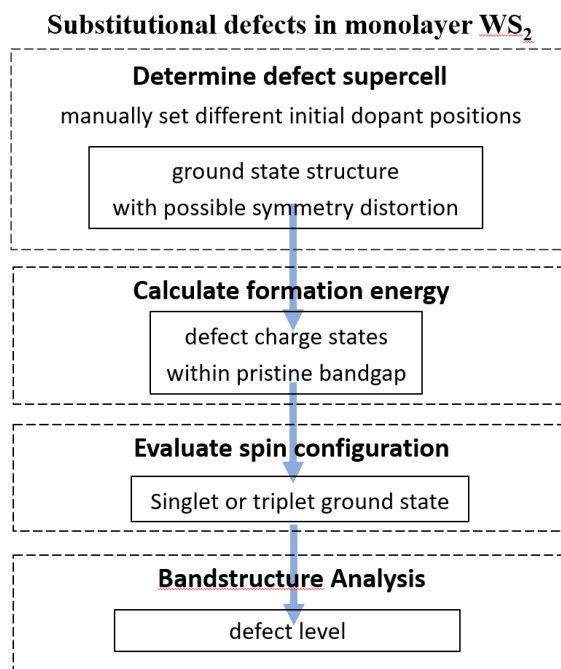


Fig. 4.1 Screening workflow

4.1 Defect Supercell

Unlike graphene, which consists of a single atomic layer, TMDs are composed of three atomic layers. These layers include a central metal atom sandwiched between chalcogenides on the top and bottom, typically forming a trigonal prismatic structure. In the 1T phase, a shift of one layer of sulfur atoms results in the S atoms adopting split positions relative to the central metal atom. For instance, in a monolayer of MoS₂, the most commonly observed polymorphs are the 1H and 1T phases. The 1H phase features trigonal prismatic coordination and belongs to the D_{3h} point group, while the 1T phase exhibits octahedral coordination and is classified under the D_{3d} point group.

When exploring defect configurational space, the energy-lowering structural distortions can be mainly categorized into four distinct motifs according to their chemical origins, as exemplified in Fig. X. For many

vacancies and interstitials, symmetry breaking was found to produce dimer bonds between undercoordinated atoms. This strong bond formation results in these distortions being highly favorable, denoted as Dimerization.

Beyond dimerization, rebonding between defect neighbors can also include replacing cation-cation/anion-anion (homoionic) bonds with more favorable cation-anion (heteroionic) bonds. This reconstruction motif is primarily observed for antisite defects, where the antisite may displace from its original position towards an oppositely-charged ion to form a new bond, while breaking a cation-cation/anion-anion bond.

For defects in materials with a stronger ionic character, crystal field effects or Jahn-Teller effects can also drive symmetry-breaking reconstructions. The crystal field effect describes the impact of the electric fields produced by the surrounding ions on the energy levels of the central ion's electrons, often leading to a redistribution of electron density and symmetry breaking. The Jahn-Teller effect occurs in certain degenerate electronic states of non-linear molecules, causing a distortion that reduces the overall energy by lifting the degeneracy.

Finally, for certain interstitial or substitutional defects, symmetry-breaking distortions can yield lower energy structures through optimizing electrostatic interactions. Compared to cation-anion rebonding, which is driven by a combination of ionic and covalent bonding interactions, no explicit new bonds are formed in this case.

Instead, the lattice electrostatic (Madelung) energy is lowered by defect rearrangement.

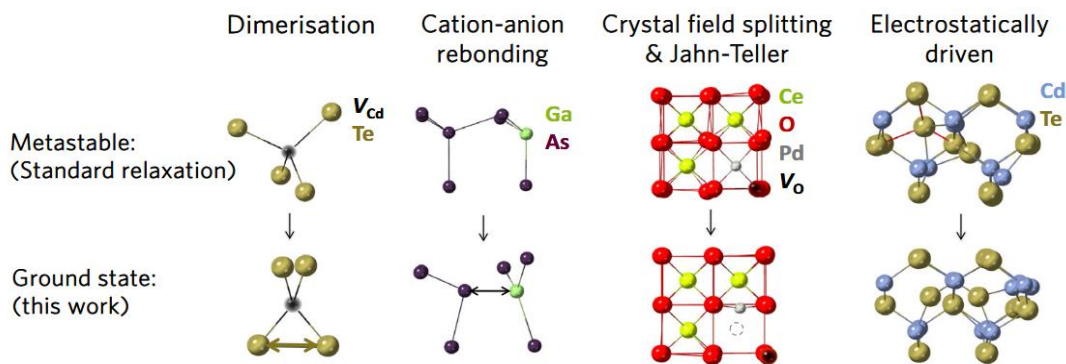


Fig. 4.1 Types of symmetry-breaking reconstructions at point defect sites identified by our method: dimerization, cation-anion rebonding, crystal field splitting and Jahn-Teller, and electrostatically driven. The high-symmetry (metastable) and symmetry-broken (ground state) structures are shown ⁶⁴

In standard geometry relaxation, the vacancy/substitution/interstitial defect configuration is initialized on a known crystal site (Wyckoff position) with all other atoms retaining their original lattice positions. Such a simple setup tends to converge to a local minimum or a saddle point on the potential energy surface along with widely implemented gradient-based optimization algorithms in DFT codes. Thus, it is necessary to actively break the local symmetry of the host crystal to enable more distorted configurations to be sampled during relaxation. In this work, we also attempt to relax the defect structures in symmetry-broken supercells but adopt a convenient approach by manually setting three initial dopant positions: one at the original W position, a second with a slight in-plane displacement, and a third with a displacement along a tilted out-of-plane direction.

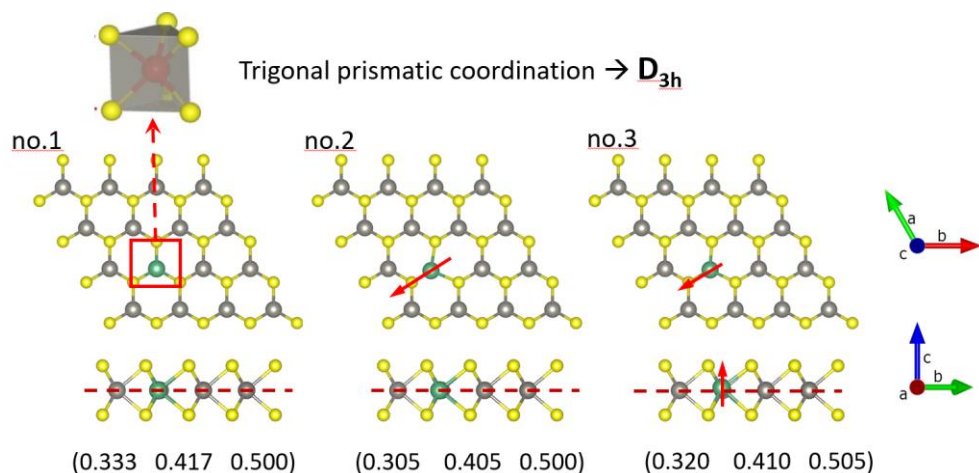


Fig. 4.2 Initial defect postions

The distribution of point groups for relaxed defect structures (in Schönflies notation) is shown here. Out of the 48 relaxed structures, approximately 80% are D_{3h} and C_{2v} , accounting for 42.2% and 35.5%, respectively. Structural distortions are widely present, with more than half of the structures reducing to point groups with lower symmetry. The subcolumns count the initial settings that yield the lowest energy geometries for each point group. For D_{3h} , all three initial coordinates consistently converge to the same configuration. However, for distorted structures, almost all lowest energy configurations are initialized by settings coordinate no. 2 and no. 3, the disrupted initial positions, whereas the first setting often traps the structure in a local minimum. This indicates that the deliberately introduced disruptions are effective.

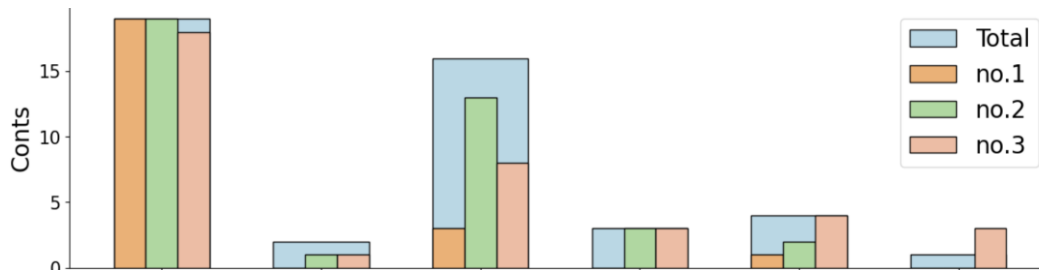


Fig. 4.3 Distribution of point groups for relaxed defect

4.2 Defect Formation Energy

The formation energy of a defect is determined by the chemical potential of everything that goes into forming the defect. While all of the different chemical potentials are interconnected, it is conceptually easier to separate them into two groups: the chemical potential of the atoms and the chemical potential of the electron. Since the electrons in the system can be manipulated after the defect is formed, the Fermi level is often considered a **free variable** and is shown as the x-axis in the formation energy diagram. The chemical potentials of the different atoms added or removed to form the defect are less dynamic and assumed to be **fixed** after the defect is formed. Therefore, what is required are the specific values of the atomic chemical potentials and the range of the Fermi level.

4.2.1 Chemical Potential Feasible Region

When a defect is introduced, atoms are exchanged with the hypothetical **atomic reservoirs** within the thermodynamics framework. The chemical potentials are defined to reflect the reservoirs for atoms that are involved in creating the defect. It should be noted that under equilibrium growth conditions there are some thermodynamic limits on the achievable values of the chemical potentials.

All of the chemical potentials are, in principle, free variables that indicate the conditions of the surrounding environment while the defect is formed. However, they are subject to specific bounds. In the following discussion we use *TM* to indicate the Transition Metal dopants.

Since the defect must form in WS_2 the chemical potentials are pinned by the plane defined by the formation of WS_2 .

$$\mu_W + 2\mu_S = E[WS_2] \quad (4.1)$$

To avoid precipitation of the elemental dopant and the host elements, the limits of the chemical potentials are also set by the stability of the elemental phases that constitute the host and defect materials. $E[A]$ is the energy per A atom in its elemental phase.

$$\begin{aligned} \mu_W &\leq E[W] \\ \mu_S &\leq E[S] \\ \mu_{Nb} &\leq E[TM] \end{aligned} \quad (4.2)$$

Moreover, **competing compounds** that shares the same elements as the defect and host material impose the boundaries of the allowed chemical potentials. Since there are no other secondary phases for tungsten (W) and sulfur (S), but there are for niobium (Nb) and sulfur (S), the following constraint can be derived:

$$x\mu_{TM} + y\mu_S \leq E[TM_xS_y] \quad (4.3)$$

Alternatively, relative chemical potentials $\Delta\mu_A = \mu_A - \mu_A^0$ can be invoked. In electronic-structure calculations, chemical potentials can be referenced to the total energy of the elemental phases at $T = 0$ K. Experimental databases employ elemental phases at standard conditions ($T = 273.15$ or 298.15 K and $P = 100$ or 101.325 kPa). Hence, equivalent constraints are established:

$$\begin{aligned} \Delta\mu_W + 2\Delta\mu_S &= \Delta E_{WS_2} \\ x\Delta\mu_{TM} + y\Delta\mu_S &\leq \Delta E_{TM_xS_y} \\ \Delta\mu_W &\leq 0 \\ \Delta\mu_S &\leq 0 \\ \Delta\mu_{TM} &\leq 0 \end{aligned} \quad (4.4)$$

Where $\Delta E[A_xB_y] = E[A_xB_y] - xE[A_x] - yE[B_y]$.

Based on relative chemical potential constraints, the **Chemical Potential Diagram (CPD)** can be determined.

The chemical potential diagram is the mathematical dual to the compositional phase diagram. To create the

diagram, convex minimization is performed in energy (E) vs. chemical potential (μ) space by taking the lower convex envelope of hyperplanes. Accordingly, “points” on the compositional phase diagram become N-dimensional convex polytopes (domains) in chemical potential space. The points of interest are usually vertex points in CPD space.

Typically, the evaluation of defect properties like formation energies only considers the boundary values of atomic chemical potentials when the system is in equilibrium with other phases. Take, for example, analyzing the O-rich limit to determine the achievable ranges for chemical potentials $\Delta\mu_{\text{Ti}}$ and $\Delta\mu_{\text{Nb}}$. Fig. 4.2a illustrates where the feasible region meets the plane at $\Delta\mu_{\text{O}} = \Delta\mu_{\text{O}}^{\text{max}}$, which indicates the upper limit of $\Delta\mu_{\text{O}}$ within the region governed by the host equation. According to Fig. 4.2a, the thermodynamic equilibrium caps $\Delta\mu_{\text{Nb}}$ at -10.35eV in the O-rich limit. Beyond this, Nb-doping would lead to the formation of Nb_2O_5 within the $C2/m$ space group. Once $\Delta\mu_{\text{O}}$ is set, $\Delta\mu_{\text{Ti}}$ is subsequently determined by the equality constraint. Fig. 4.2b depicts another boundary scenario where the feasible region intersects with the $\Delta\mu_{\text{Nb}} = 0$ plane in the Nb-rich limit, confining $\Delta\mu_{\text{Ti}}$ and $\Delta\mu_{\text{O}}$ to a limited range, as detailed in Table 1. Outside this specified range, compounds like Ti_2O and Ti_3O_5 would begin to form⁵³.

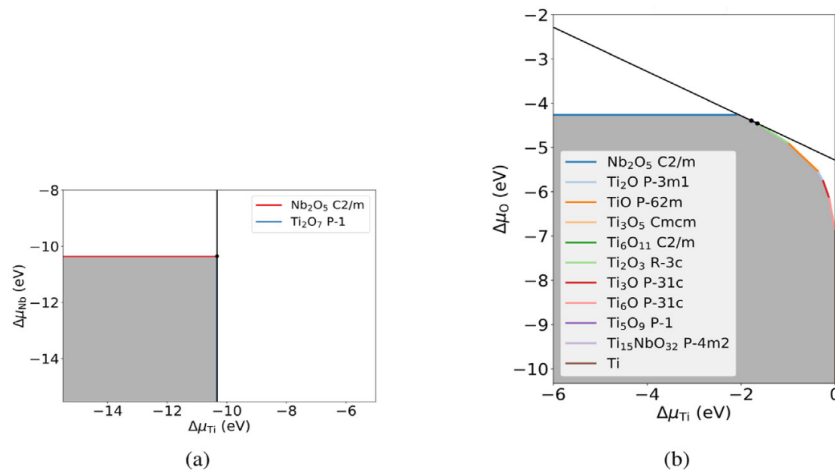


Fig. 4.4 Intersection of the feasible region of anatase $\text{TiO}_2\text{:Nb}$ with: (a) the $\Delta\mu_{\text{O}} = \Delta\mu_{\text{max O}} = -0.12\text{ eV}$ plane; (b) the $\Delta\mu_{\text{Nb}} = 0\text{ eV}$ plane. The gray area represents the inequalities constraints and the bold black line the equality constraint.

In a system with N components, the chemical potential space spans $N - 1$ dimensions, allowing exploration of all possible intrinsic properties of the material. Consider the ternary compound ZrNiSn , which has two dimensions of chemical potential defining the feasible chemical conditions for intrinsic ZrNiSn . The chemical potential space for ZrNiSn is depicted in Fig. 4.4c. The range of possible chemical potentials is constrained by endpoints marked by letters, which align with three-phase equilibria represented as triangles in an isothermal phase diagram shown in Fig. 4.4b, along with chemical potential points of interest (typically associated with multiphase equilibria).

ZrNiSn can achieve equilibrium with eight different phases, each dictating distinct extreme chemical conditions. These conditions usually result in different intrinsic defect concentrations. The potential extrema of all defect concentrations can be qualitatively predicted by employing simple thermodynamic principles, using the phase diagram in Fig. Xb alone. A Brouwer diagram connecting all 8 points is illustrated in Fig. 4a on a 2-dimensional plot by navigating between adjacent three-phase equilibria that involve ZrNiSn (as identified in Fig. 4.4b). This visualization technique is termed a Brouwer band diagram, analogous to an electronic band diagram where a path through special points in the Brillouin zone is traced to follow the variation in electronic state energy. This pathway of chemical conditions $A \rightarrow B \rightarrow C \rightarrow D \rightarrow E \rightarrow F \rightarrow G \rightarrow H$, along which the defect properties are charted, is displayed in the chemical potential space in Fig. Xc. Experimentally, these varied phase regions can be explored through phase boundary mapping, potentially revealing new material properties such as high-efficiency thermoelectric materials like Mg_3Sb_2 , ZnSb , and TiNiSn .

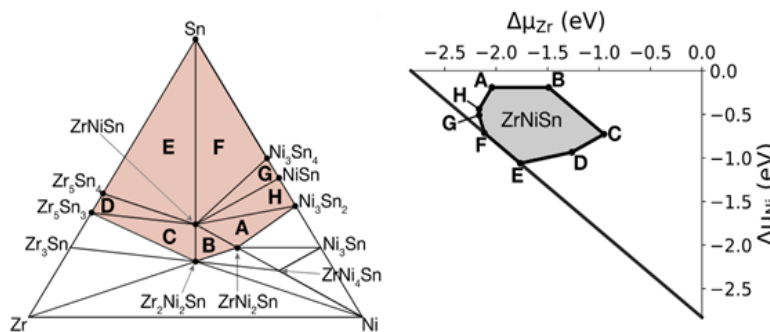


Fig. 4.5 Two representatives for chemical potential space ⁶⁵

Here calculations were performed using the first set of constraints. The solved μ can be directly incorporated into the formation energy formula. We will discuss how the limiting values of chemical potential are determined for Nb defect.

Step 1: We can retrieve the stable structures of all relevant elemental phases and competing compounds from the **Materials Project Database (MPD)**. Total energies are calculated in VASP to derive the energy per formula unit. The results are presented in the table below, with units in electron volts (eV).

Tab. 4.1 Calculated energies of related elemental and compound phases

E[W]	E[S]	E[Nb]	E[WS ₂]	E[Nb ₂]	E[NbS ₃]	E[Nb ₃ S ₅]	E[Nb ₃ S ₄]
-12.866	-4.089	-10.272	-23.667	-21.624	-25.755	-60.511	-55.173

Step 2: Limiting values of the chemical potentials. Defect formation energies are usually reported for the extreme conditions; in this case:

- S-rich conditions, where μ_S achieves its maximum value $E[S]$;
- W-rich conditions, where μ_W achieves its maximum values $E[W]$.

Considering the equation:

$$\mu_W + 2\mu_S = E[WS_2] \quad (4.5)$$

The following chemical potentials are solved:

$$\begin{array}{ll} \text{S-rich} & : \mu_S = -4.089\text{eV} \quad \mu_W = -15.489\text{eV} \\ \text{W-rich} & : \mu_W = -12.866\text{eV} \quad \mu_S = -5.401\text{eV} \end{array} \quad (4.6)$$

Step3: The limiting values of μ_{Nb} are to be calculated based on the inequalities determined by multiple competing phases under S-rich and S-poor conditions. The minimum value is selected, as it indicates the most stable compounds under the given S condition, as displayed in table below.

Tab. 4.2 Chemical potential of Nb defect in competing phases

Species	$E[Nb_xS_y]$	μ_{Nb} S-rich	μ_{Nb} W-rich
Nb_3S_4	-55.173	-12.939 eV	-11.191 eV
Nb_3S_5	-60.511	-13.355 eV	-11.170 eV
NbS_2	-21.625	-13.447 eV	-10.825 eV
NbS_3	-25.755	- 13.488 eV	-9.555 eV

Hence the atom chemical potential term in Formation energy can be derived:

$$\sum n_i \mu_i = 1\mu_W - 1\mu_{Nb} = \begin{cases} -15.489 - (-13.488) = -2.001\text{eV} & \text{S rich} \\ -12.866 - (-11.191) = -1.675\text{eV} & \text{W rich} \end{cases} \quad (4.7)$$

Finally, the chemical potential range can be determined as plotted in Fig. 4.6.

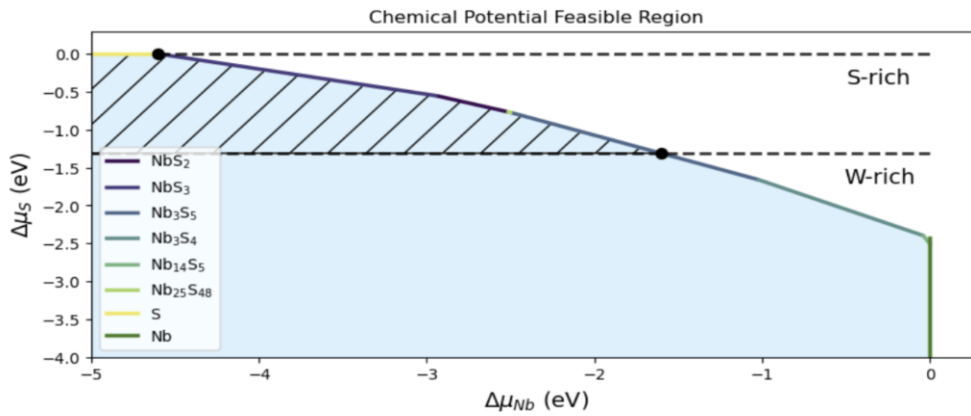


Fig. 4.6. Chemical potential feasible region for Nb defect.

4.2.2 Charge Correction

In supercell approach, the isolated defect is replaced by a **periodic array of defects**. Such a periodic array contains unrealistically large defect concentrations, resulting in artificial interactions between the defects : Overlap of the wavefunctions, elastic interactions, electrostatic interactions and magnetic interactions. The focus of this contribution are the electrostatic interactions which typically dominate. Specifically, when the supercell is adopted under the periodic boundary condition, the total energies for charged defects are not properly estimated due to interactions between a defect, its images, and background charge. Therefore, we need to correct the total energies of the charged defect supercells to those in the **dilutie limit**. For this purpose, **Freysoldt-Neugebauer-Van de Walle (FNV) correction** was introduced.

The FNV finite-size correction can work only with the electrostatic potentials from the DFT calculations and the dielectric constant of the material. The alignment-like term in the original Freysoldt correction paper requires the short-range potential ($V_{q/0}^{sr}$) to be shifted by a constant value (C) so that the potential is effectively zero far away from the defect. Fig. X shows the planar-averaged values of the different potentials involved in calculating the FNV charge-state correction. The long-range (black) term is computed from a Gaussian model, the potential difference (red) and short-range terms are both shifted so the origin is at the defect positions identified before. The difference in electrostatic potentials between the defect and pristine cells and the short-range potential are both directly computed from the files storing the electrostatic potential information (e.g. LOCPOT files for VASP calculations). The position of the defect was automatically determined and can be validated by the fact that the potential difference and short-range potential profile both peak at the origin. This method models the defect charge normally as a Gaussian distribution.

The difference between the electrostatic potential of the charged defect and perfect bulk supercells, calculated far from the defect, is aligned with the defect model potential.

$$\Delta E^{\text{model}} = E_{Q/\text{slabs}}^{\text{model}} - E_{Q/\text{surface}}^{\text{model}} \quad (4.10)$$

$$\Delta V^{\text{DFT}} = V^{\text{DFT}}(\text{slab} + \text{defect}) - V^{\text{DFT}}(\text{slab}) \quad (4.11)$$

For the potential alignment

$$\Delta V^{\text{DFT}} - C - V_{Q/\text{slabs}}^{\text{model}} \rightarrow 0 \quad \text{away from defect} \quad (4.12)$$

$$\Delta E^{\text{corr}} = \Delta E^{\text{model}} + QC \quad (4.13)$$

$$\begin{aligned} \Delta E^{\text{corr}} &= E_{\text{model}}^{\text{iso}} - E_{\text{model}}^{\text{periodic}} + QC \\ \Delta V^{\text{DFT}} &= V^{\text{DFT}}(\text{defect}) - V^{\text{DFT}}(\text{pristine}) \\ \Delta V^{\text{DFT}} - C - E_{\text{model}}^{\text{periodic}} &\rightarrow 0 \quad \text{away from defect} \end{aligned} \quad (4.14)$$

The correction simplifies to a periodicity correction and an alignment-like term. In code practice, we utilize the post-analysis tool `sxdefectalign2d`. The `sxdefectalign2d` program, which implements the Poisson solver, is interfaced to the potential format of several common DFT programs. For VASP, it is necessary to provide the LOCPOT file and the dielectric tensor.

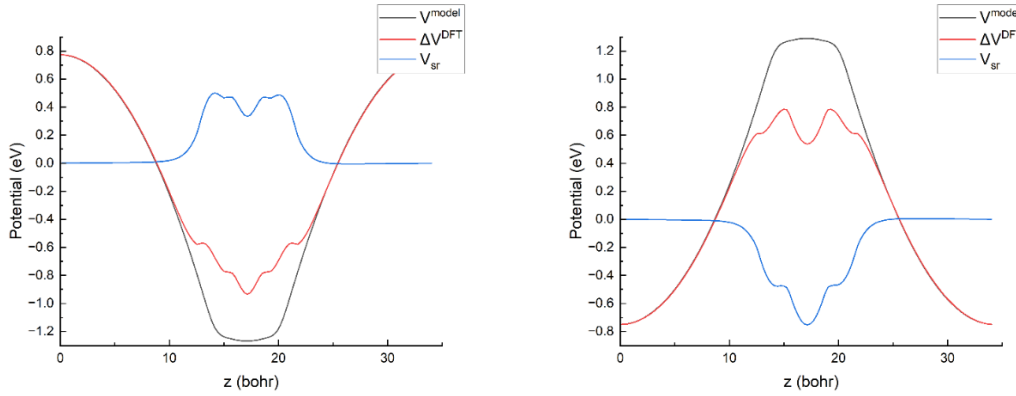


Fig. 4.7 Planar-averaged potentials before and after alignment from the FNV charge-state correction b

The left and right figures represent the correction for charge states +1 and -1, respectively. It is observable that the V_{sr} approaches zero far from the defect position ($z=17.1$ bohr), which aligns with the check conditions required by `sxdefectalign2d`.

4.2.3 Formation Energies and Charge Transition Level

As each term determined in the formation energy formula mentioned in section 3, the specific values are calculated in Tab. 4.3 by locating fermi level at VBM.

Tab. 4.3 Formation energies of Nb

Defect	q	$E_{D,q} - E_{Host}$	qE_{VBM}	$\sum n_i \mu_i$ (S-rich/W-rich)	E_{corr}	$E_f(E_F=VBM)$ (S-rich/W-rich)
Nb_W^{+1}	+1	4.076	-1.518	-2.001/-1.675	0.094	0.651/0.977
Nb_W^0	0	2.232	0	-2.001/-1.675	0	0.231/0.557
Nb_W^{-1}	-1	1.098	1.518	-2.001/-1.675	0.071	0.686/1.012

The defect thermodynamic charge transition levels are defined by the value of E_F for which two defect charge states have the same formation energy.

Under S rich condition:

$$E_{D,q}^f(E_F) = \begin{cases} 4.076 - 1.158 - 2.001 + E_F & q=+1 \\ 2.23 - 1.158 & q=0 \\ 1.098 + 1.158 - 2.001 - E_F & q=-1 \end{cases} \quad (4.15)$$

The corresponding formation energy diagram:

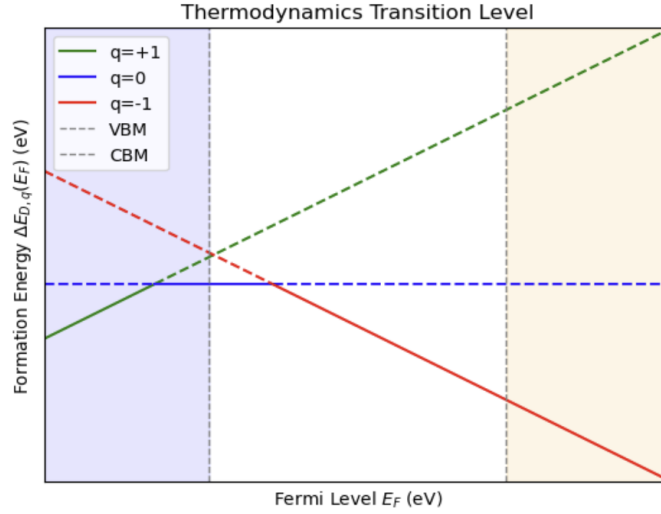


Fig. 4.5 Formation Energy Diagram of Nb defect

Fig. 4.5 above illustrates that the Nb_W defect can exist in two charge states, namely, neutral ($q = 0$) and singly negatively charged ($q = -1$). Their crossing point stands $\epsilon(0/-1) = 0.386\text{eV}$ (referenced to the VBM) for **thermodynamic transition level**, where the defect goes from one equilibrated configuration with charge state $q=0$ to a different configuration with charge state $q=-1$.

The calculated results can be compared with the formation energy values by Bruno Schuler et al. Defects like Cr_W and Mo_W are of a similar type. A similar results should be expected for Nb_W . When fermi level equals to VBM, this work reports formation energy values of 0.557eV and 0.231eV for Nb_W , which are aligned with the existing results. The calculations in this work above are likely to be correct.

The formalism is applied to consider all 4d and 5d transition metal elements as substitutional defects, displayed in Fig. 4.6

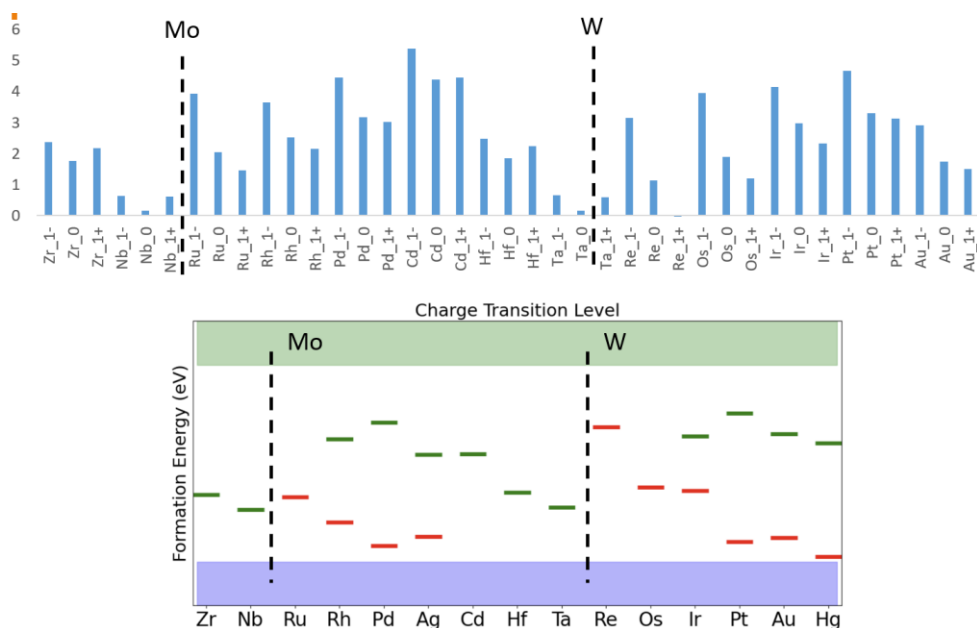


Fig. 4.6 Defect formation energies and charge transition levels in 4d and 5d transition metals. Mo and W are marked with vertical dotted lines

With determined spin triplet ground state defect, the relaxed local configurations of them are examined. The distance between sulfur atoms is measured to assess the in-plane strain, with the S-S distance in pristine geometry being 3.19 angstroms. While the neutral Hg and Cd defects retain the D_{3h} point group symmetry, they exhibit a relatively large tensile strain. In contrast, the Rh defect in the +1 charge state displays a reduced symmetry C_s and experiences considerably less tensile strain. This observation demonstrates that distortion cannot be solely characterized by point group symmetry.

4.3 Spin-triplet Ground State

As spin triplet system are necessary for potential spin qubits, the ground state spin multiplicity is examined for all possible charged defects. Three of them exhibit triplet ground state: Rh^{1+} , Hg^0 and Cd^0 . Notably, for these three triplet ground defect, their relaxed local configurations are checked here. Distance between sulfur atoms are measured to assess the in-plane strain. The S-S distance is 3.19 angstrom in pristine geometry. Although the neutral Hg and Cd defect maintain the D_{3h} point group symmetry, they exhibit a relatively large tensile

strain. The Rh defect in charge state +1 have a reduced symmetry C_s , but it present a much weaker tensile strain. This observation may indicate that distortion cannot be characterized only by point group symmetry.

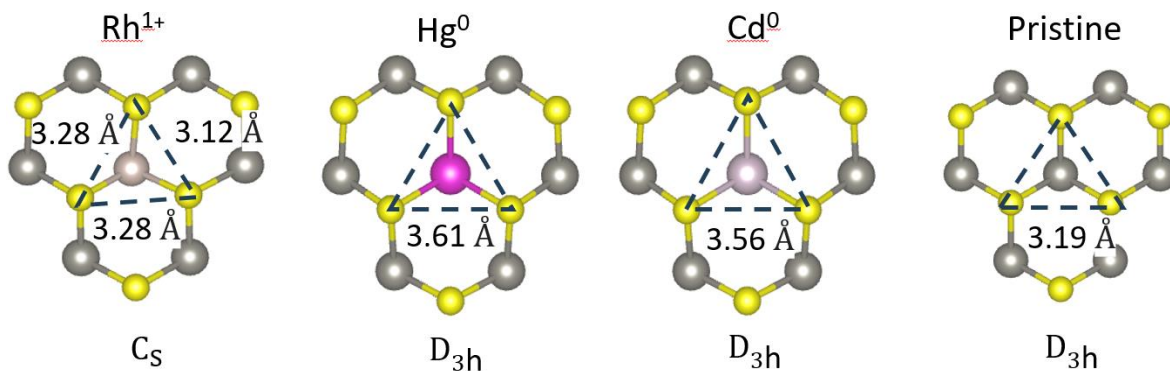


Fig. 4.7 In-plane strain for triplet ground state structure

The single particle bandstructures are calculated to identify the defect levels. The defect levels are recognized by projection to each atoms.

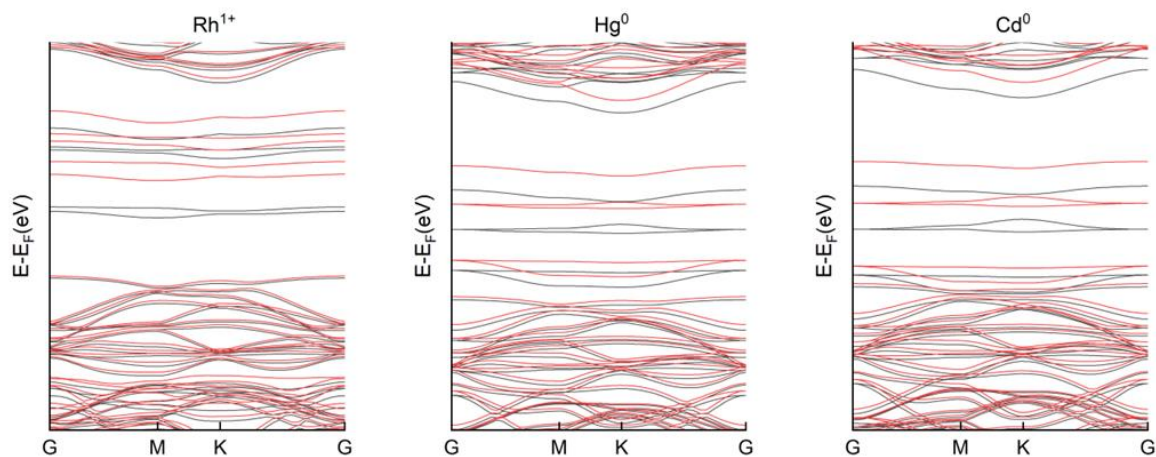


Fig. 4.7 Calculated band structure of triplet ground state defects

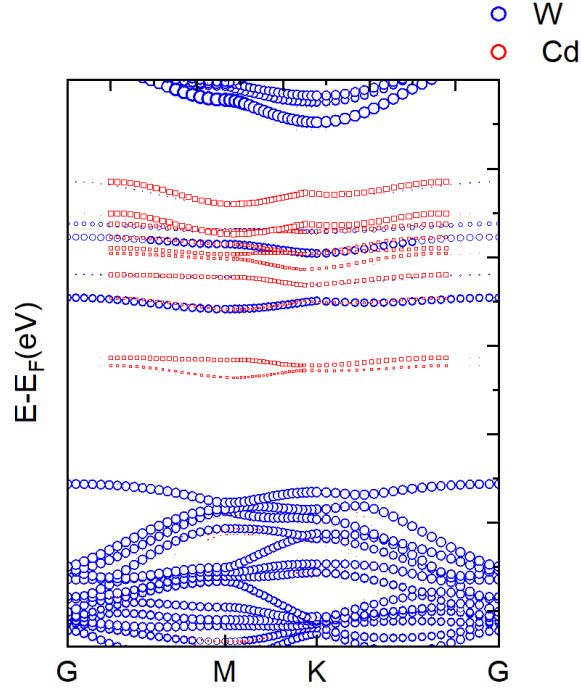


Fig. 4.8 Projected bandstructure for Rh^{1+} defect

5 Summary

In this report, we have focused on color centers in solids, which serve as a promising host material platform for quantum information technology due to their distinctly advantageous properties. Beyond the prototype NV center, numerous promising solid-state defect systems are reviewed and summarized in Section 2 to provide inspiration. For TMD materials, while their potential as a new generation of semiconductors is well recognized, their role as quantum point defects has not received sufficient attention. Section 3 summarizes the key quantities essential for quantum applications and their methodologies using DFT. Building on the representative research cases and first-principles methods discussed in Sections 2 and 3, this work investigates potential candidates for substitutional quantum defects in 2D WS₂. Although the analysis is limited to evaluating basic ground state properties such as

symmetry and formation energies, only three spin triplet ground state defects were identified from all 4d and 5d transition metal elements as dopants in various charge states. The efforts detailed in Section 4 establish a solid foundation for further studies.

6 Reference

- (1) Steger, M.; Saeedi, K.; Thewalt, M. L. W.; Morton, J. J. L.; Riemann, H.; Abrosimov, N. V.; Becker, P.; Pohl, H.-J. Quantum Information Storage for over 180 s Using Donor Spins in a ^{28}Si “Semiconductor Vacuum.” *Science* **2012**, 336 (6086), 1280–1283. <https://doi.org/10.1126/science.1217635>.
- (2) Zhang, G.; Cheng, Y.; Chou, J.-P.; Gali, A. Material Platforms for Defect Qubits and Single-Photon Emitters. *Applied Physics Reviews* **2020**, 7 (3), 031308. <https://doi.org/10.1063/5.0006075>.
- (3) Bassett, L. C.; Alkauskas, A.; Exarhos, A. L.; Fu, K.-M. C. Quantum Defects by Design. *Nanophotonics* **2019**, 8 (11), 1867–1888. <https://doi.org/10.1515/nanoph-2019-0211>.
- (4) *Emerging Spintronic Materials and Functionalities - Guo - 2024 - Advanced Materials - Wiley Online Library*. <https://onlinelibrary.wiley.com/doi/10.1002/adma.202301854> (accessed 2024-06-18).
- (5) Lilieholm, J. F.; Niaouris, V.; Kato, A.; Fu, K.-M. C.; Blinov, B. B. Photon-Mediated Entanglement Scheme between a ZnO Semiconductor Defect and a Trapped Yb Ion. *Applied Physics Letters* **2020**, 117 (15), 154002. <https://doi.org/10.1063/5.0019892>.
- (6) Zhou, Y.; Wang, Z.; Rasmita, A.; Kim, S.; Berhane, A.; Bodrog, Z.; Adamo, G.; Gali, A.; Aharonovich, I.; Gao, W.-B. Room Temperature Solid-State Quantum Emitters in the Telecom Range. *Sci Adv* **2018**, 4 (3), eaar3580. <https://doi.org/10.1126/sciadv.aar3580>.
- (7) He, Y.-M.; Clark, G.; Schaibley, J. R.; He, Y.; Chen, M.-C.; Wei, Y.-J.; Ding, X.; Zhang, Q.; Yao, W.; Xu, X.; Lu, C.-Y.; Pan, J.-W. Single Quantum Emitters in Monolayer Semiconductors. *Nature Nanotech* **2015**, 10 (6), 497–502. <https://doi.org/10.1038/nnano.2015.75>.
- (8) Abdi, M.; Chou, J.-P.; Gali, A.; Plenio, M. B. Color Centers in Hexagonal Boron Nitride Monolayers: A Group Theory and Ab Initio Analysis. *ACS Photonics* **2018**, 5 (5), 1967–1976. <https://doi.org/10.1021/acsphotonics.7b01442>.
- (9) Sipahigil, A.; Evans, R. E.; Sukachev, D. D.; Burek, M. J.; Borregaard, J.; Bhaskar, M. K.; Nguyen, C. T.; Pacheco, J. L.; Atikian, H. A.; Meuwly, C.; Camacho, R. M.; Jelezko, F.; Bielejec, E.; Park, H.; Lončar, M.; Lukin, M. D. An Integrated Diamond Nanophotonics Platform for Quantum-Optical Networks. *Science* **2016**, 354 (6314), 847–850. <https://doi.org/10.1126/science.aah6875>.
- (10) Evans, D. A.; Stempel, A. V.; Vale, R.; Ruehle, S.; Lefler, Y.; Branco, T. A Synaptic Threshold Mechanism for Computing Escape Decisions. *Nature* **2018**, 558 (7711), 590–594. <https://doi.org/10.1038/s41586-018-0244-6>.

- (11) Koehl, W. F.; Seo, H.; Galli, G.; Awschalom, D. D. Designing Defect Spins for Wafer-Scale Quantum Technologies. *MRS Bulletin* **2015**, *40* (12), 1146–1153. <https://doi.org/10.1557/mrs.2015.266>.
- (12) Jhuria, K.; Ivanov, V.; Polley, D.; Zhiyenbayev, Y.; Liu, W.; Persaud, A.; Redjem, W.; Qarony, W.; Parajuli, P.; Ji, Q.; Gonsalves, A. J.; Bokor, J.; Tan, L. Z.; Kanté, B.; Schenkel, T. Programmable Quantum Emitter Formation in Silicon. *Nat Commun* **2024**, *15* (1), 4497. <https://doi.org/10.1038/s41467-024-48714-2>.
- (13) Borlido, P.; Schmidt, J.; Huran, A. W.; Tran, F.; Marques, M. A. L.; Botti, S. Exchange-Correlation Functionals for Band Gaps of Solids: Benchmark, Reparametrization and Machine Learning. *npj Comput Mater* **2020**, *6* (1), 1–17. <https://doi.org/10.1038/s41524-020-00360-0>.
- (14) Jeske, J.; Lau, D. W. M.; Vidal, X.; McGuinness, L. P.; Reineck, P.; Johnson, B. C.; Doherty, M. W.; McCallum, J. C.; Onoda, S.; Jelezko, F.; Ohshima, T.; Volz, T.; Cole, J. H.; Gibson, B. C.; Greentree, A. D. Stimulated Emission from Nitrogen-Vacancy Centres in Diamond. *Nat Commun* **2017**, *8* (1), 14000. <https://doi.org/10.1038/ncomms14000>.
- (15) Ivády, V.; Abrikosov, I. A.; Gali, A. First Principles Calculation of Spin-Related Quantities for Point Defect Qubit Research. *npj Comput Mater* **2018**, *4* (1), 1–13. <https://doi.org/10.1038/s41524-018-0132-5>.
- (16) Goldman, M. L.; Doherty, M. W.; Sipahigil, A.; Yao, N. Y.; Bennett, S. D.; Manson, N. B.; Kubanek, A.; Lukin, M. D. State-Selective Intersystem Crossing in Nitrogen-Vacancy Centers. *Phys. Rev. B* **2015**, *91* (16), 165201. <https://doi.org/10.1103/PhysRevB.91.165201>.
- (17) Miller, B. S.; Bezing, L.; Gliddon, H. D.; Huang, D.; Dold, G.; Gray, E. R.; Heaney, J.; Dobson, P. J.; Nastouli, E.; Morton, J. J. L.; McKendry, R. A. Spin-Enhanced Nanodiamond Biosensing for Ultrasensitive Diagnostics. *Nature* **2020**, *587* (7835), 588–593. <https://doi.org/10.1038/s41586-020-2917-1>.
- (18) Dutt, M. V. G.; Childress, L.; Jiang, L.; Togan, E.; Maze, J.; Jelezko, F.; Zibrov, A. S.; Hemmer, P. R.; Lukin, M. D. Quantum Register Based on Individual Electronic and Nuclear Spin Qubits in Diamond. *Science* **2007**, *316* (5829), 1312–1316. <https://doi.org/10.1126/science.1139831>.
- (19) Awschalom, D. D.; Hanson, R.; Wrachtrup, J.; Zhou, B. B. Quantum Technologies with Optically Interfaced Solid-State Spins. *Nature Photon* **2018**, *12* (9), 516–527. <https://doi.org/10.1038/s41566-018-0232-2>.
- (20) Li, L.; Santis, L. D.; Harris, I. B. W.; Chen, K. C.; Gao, Y.; Christen, I.; Choi, H.; Trusheim, M.; Song, Y.; Errando-Herranz, C.; Du, J.; Hu, Y.; Clark, G.; Ibrahim, M. I.; Gilbert, G.; Han, R.; Englund, D. Heterogeneous Integration of Spin–Photon Interfaces with a CMOS Platform. *Nature* **2024**, *630* (8015), 70–76. <https://doi.org/10.1038/s41586-024-07371-7>.
- (21) Gali, A.; Maze, J. R. Ab Initio Study of the Split Silicon-Vacancy Defect in Diamond: Electronic Structure and Related Properties. *Phys. Rev. B* **2013**, *88* (23), 235205. <https://doi.org/10.1103/PhysRevB.88.235205>.

- (22) Jahnke, K. D.; Sipahigil, A.; Binder, J. M.; Doherty, M. W.; Metsch, M.; Rogers, L. J.; Manson, N. B.; Lukin, M. D.; Jelezko, F. Electron–Phonon Processes of the Silicon-Vacancy Centre in Diamond. *New J. Phys.* **2015**, *17* (4), 043011. <https://doi.org/10.1088/1367-2630/17/4/043011>.
- (23) Thiering, G.; Gali, A. Ab Initio Magneto-Optical Spectrum of Group-IV Vacancy Color Centers in Diamond. *Phys. Rev. X* **2018**, *8* (2), 021063. <https://doi.org/10.1103/PhysRevX.8.021063>.
- (24) Choi, S.; Tran, T. T.; Elbadawi, C.; Lobo, C.; Wang, X.; Juodkazis, S.; Seniutinas, G.; Toth, M.; Aharonovich, I. Engineering and Localization of Quantum Emitters in Large Hexagonal Boron Nitride Layers. *ACS Appl. Mater. Interfaces* **2016**, *8* (43), 29642–29648. <https://doi.org/10.1021/acsami.6b09875>.
- (25) Deokar, G.; Jin, J.; Schwingenschlögl, U.; Costa, P. M. F. J. Chemical Vapor Deposition-Grown Nitrogen-Doped Graphene’s Synthesis, Characterization and Applications. *npj 2D Mater Appl* **2022**, *6* (1), 1–17. <https://doi.org/10.1038/s41699-022-00287-8>.
- (26) Wang, M.; Sun, H.; Ye, X.; Yu, P.; Liu, H.; Zhou, J.; Wang, P.; Shi, F.; Wang, Y.; Du, J. Self-Aligned Patterning Technique for Fabricating High-Performance Diamond Sensor Arrays with Nanoscale Precision. *Science Advances* **2022**, *8* (38), eabn9573. <https://doi.org/10.1126/sciadv.abn9573>.
- (27) Weber, J. R.; Koehl, W. F.; Varley, J. B.; Janotti, A.; Buckley, B. B.; Van De Walle, C. G.; Awschalom, D. D. Quantum Computing with Defects. *Proc. Natl. Acad. Sci. U.S.A.* **2010**, *107* (19), 8513–8518. <https://doi.org/10.1073/pnas.1003052107>.
- (28) Hornos, T.; Gali, A.; Svensson, B. G. Large-Scale Electronic Structure Calculations of Vacancies in 4H-SiC Using the Heyd-Scuseria-Ernzerhof Screened Hybrid Density Functional. arXiv May 16, 2011. <https://doi.org/10.48550/arXiv.1105.3079>.
- (29) Wang, J.-F.; Yan, F.-F.; Li, Q.; Liu, Z.-H.; Liu, H.; Guo, G.-P.; Guo, L.-P.; Zhou, X.; Cui, J.-M.; Wang, J.; Zhou, Z.-Q.; Xu, X.-Y.; Xu, J.-S.; Li, C.-F.; Guo, G.-C. Coherent Control of Nitrogen-Vacancy Center Spins in Silicon Carbide at Room Temperature. *Phys. Rev. Lett.* **2020**, *124* (22), 223601. <https://doi.org/10.1103/PhysRevLett.124.223601>.
- (30) Baumberg, J. J.; Aizpurua, J.; Mikkelsen, M. H.; Smith, D. R. Extreme Nanophotonics from Ultrathin Metallic Gaps. *Nat. Mater.* **2019**, *18* (7), 668–678. <https://doi.org/10.1038/s41563-019-0290-y>.
- (31) von Bardeleben, H. J.; Cantin, J. L.; Csore, A.; Gali, A.; Rauls, E.; Gerstmann, U. NV Centers in 3C, 4H, and 6H Silicon Carbide: A Variable Platform for Solid-State Qubits and Nanosensors. *PHYSICAL REVIEW B* **2016**, *94* (12). <https://doi.org/10.1103/PhysRevB.94.121202>.
- (32) Butler, S. Z.; Hollen, S. M.; Cao, L.; Cui, Y.; Gupta, J. A.; Gutiérrez, H. R.; Heinz, T. F.; Hong, S. S.; Huang, J.; Ismach, A. F.; Johnston-Halperin, E.; Kuno, M.; Plashnitsa, V. V.; Robinson, R. D.; Ruoff, R. S.; Salahuddin, S.; Shan, J.; Shi, L.; Spencer, M. G.; Terrones, M.; Windl, W.; Goldberger, J. E. Progress, Challenges, and Opportunities in Two-Dimensional Materials Beyond Graphene. *ACS Nano* **2013**, *7* (4), 2898–2926. <https://doi.org/10.1021/nn400280c>.
- (33) Liu, X.; Hersam, M. C. 2D Materials for Quantum Information Science. *Nat Rev Mater* **2019**, *4* (10), 669–684. <https://doi.org/10.1038/s41578-019-0136-x>.

- (34) Huang, P.; Grzeszczyk, M.; Vaklinova, K.; Watanabe, K.; Taniguchi, T.; Novoselov, K. S.; Koperski, M. Carbon and Vacancy Centers in Hexagonal Boron Nitride. *Phys. Rev. B* **2022**, *106* (1), 014107. <https://doi.org/10.1103/PhysRevB.106.014107>.
- (35) Tran, T. T.; Bray, K.; Ford, M. J.; Toth, M.; Aharonovich, I. Quantum Emission from Hexagonal Boron Nitride Monolayers. *Nature Nanotech* **2016**, *11* (1), 37–41. <https://doi.org/10.1038/nnano.2015.242>.
- (36) Bulancea-Lindvall, O.; Son, N. T.; Abrikosov, I. A.; Ivády, V. Dipolar Spin Relaxation of Divacancy Qubits in Silicon Carbide. *npj Comput Mater* **2021**, *7* (1), 1–11. <https://doi.org/10.1038/s41524-021-00673-8>.
- (37) Maciaszek, M.; Razinkovas, L.; Alkauskas, A. Thermodynamics of Carbon Point Defects in Hexagonal Boron Nitride. *Phys. Rev. Mater.* **2022**, *6* (1), 014005. <https://doi.org/10.1103/PhysRevMaterials.6.014005>.
- (38) Manzeli, S.; Ovchinnikov, D.; Pasquier, D.; Yazyev, O. V.; Kis, A. 2D Transition Metal Dichalcogenides. *Nat Rev Mater* **2017**, *2* (8), 17033. <https://doi.org/10.1038/natrevmats.2017.33>.
- (39) Sun Z.-H.; Guan H.-M.; Fu L.; Shen B.; Tang N.; State Key Laboratory of Artificial Microstructure and Mesoscopic Physics, Peking University, Beijing 100871, China. Valleytronic properties and devices based on two-dimensional atomic layer materials. *Acta Phys. Sin.* **2021**, *70* (2), 027302. <https://doi.org/10.7498/aps.70.20201415>.
- (40) Vannucci, L.; Neto, J. F.; Piccinini, C.; Paralikis, A.; Gregersen, N.; Munkhbat, B. Single-Photon Emitters in WSe₂: The Critical Role of Phonons on Excitation Schemes and Indistinguishability. arXiv March 15, 2024. <http://arxiv.org/abs/2402.10897> (accessed 2024-05-15).
- (41) Miwa, J. A.; Ulstrup, S.; Sørensen, S. G.; Dendzik, M.; ifmmode \checkC\else Č\fiabo, A. G. \checks\else š\fiifmmode \acute{e}\else é\fi; Bianchi, M.; Lauritsen, J. V.; Hofmann, P. Electronic Structure of Epitaxial Single-Layer \mathrm{MoS}_2. *Phys. Rev. Lett.* **2015**, *114* (4), 046802. <https://doi.org/10.1103/PhysRevLett.114.046802>.
- (42) Li, S.; Thiering, G.; Udvarhelyi, P.; Ivády, V.; Gali, A. Carbon Defect Qubit in Two-Dimensional WS₂. *Nat Commun* **2022**, *13* (1), 1210. <https://doi.org/10.1038/s41467-022-28876-7>.
- (43) Tsai, J.-Y.; Pan, J.; Lin, H.; Bansil, A.; Yan, Q. Antisite Defect Qubits in Monolayer Transition Metal Dichalcogenides. *Nat Commun* **2022**, *13* (1), 492. <https://doi.org/10.1038/s41467-022-28133-x>.
- (44) Aharonovich, I.; Englund, D.; Toth, M. Solid-State Single-Photon Emitters. *Nature Photon* **2016**, *10* (10), 631–641. <https://doi.org/10.1038/nphoton.2016.186>.
- (45) Afzelius, M.; Gisin, N.; de Riedmatten, H. Quantum Memory for Photons. *Physics Today* **2015**, *68* (12), 42–47. <https://doi.org/10.1063/PT.3.3021>.
- (46) Raha, M.; Chen, S.; Phenicie, C. M.; Ourari, S.; Dibos, A. M.; Thompson, J. D. Optical Quantum Nondemolition Measurement of a Single Rare Earth Ion Qubit. *Nat Commun* **2020**, *11* (1), 1605. <https://doi.org/10.1038/s41467-020-15138-7>.

- (47) Thomas, J. C.; Chen, W.; Xiong, Y.; Barker, B. A.; Zhou, J.; Chen, W.; Rossi, A.; Kelly, N.; Yu, Z.; Zhou, D.; Kumari, S.; Barnard, E. S.; Robinson, J. A.; Terrones, M.; Schwartzberg, A.; Ogletree, D. F.; Rotenberg, E.; Noack, M. M.; Griffin, S.; Raja, A.; Strubbe, D. A.; Rignanese, G.-M.; Weber-Bargioni, A.; Hautier, G. A Substitutional Quantum Defect in WS₂ Discovered by High-Throughput Computational Screening and Fabricated by Site-Selective STM Manipulation. *Nat Commun* **2024**, *15* (1), 3556. <https://doi.org/10.1038/s41467-024-47876-3>.
- (48) Bertoldo, F.; Ali, S.; Manti, S.; Thygesen, K. S. Quantum Point Defects in 2D Materials - the QPOD Database. *npj Comput Mater* **2022**, *8* (1), 56. <https://doi.org/10.1038/s41524-022-00730-w>.
- (49) Frey, N. C.; Akinwande, D.; Jariwala, D.; Shenoy, V. B. Machine Learning-Enabled Design of Point Defects in 2D Materials for Quantum and Neuromorphic Information Processing. *ACS Nano* **2020**, *14* (10), 13406–13417. <https://doi.org/10.1021/acsnano.0c05267>.
- (50) Broberg, D.; Bystrom, K.; Srivastava, S.; Dahliah, D.; Williamson, B. A. D.; Weston, L.; Scanlon, D. O.; Rignanese, G.-M.; Dwaraknath, S.; Varley, J.; Persson, K. A.; Asta, M.; Hautier, G. High-Throughput Calculations of Charged Point Defect Properties with Semi-Local Density Functional Theory—Performance Benchmarks for Materials Screening Applications. *npj Comput Mater* **2023**, *9* (1), 72. <https://doi.org/10.1038/s41524-023-01015-6>.
- (51) Shen, J.-X.; Voss, L. F.; Varley, J. B. Simulating Charged Defects at Database Scale. arXiv March 8, 2024. <http://arxiv.org/abs/2403.05689> (accessed 2024-03-24).
- (52) Huang, M.; Zheng, Z.; Dai, Z.; Guo, X.; Wang, S.; Jiang, L.; Wei, J.; Chen, S. DASP: Defect and Dopant Ab-Initio Simulation Package. *J. Semicond.* **2022**, *43* (4), 042101. <https://doi.org/10.1088/1674-4926/43/4/042101>.
- (53) Arrigoni, M.; Madsen, G. K. H. Spinney: Post-Processing of First-Principles Calculations of Point Defects in Semiconductors with Python. *Computer Physics Communications* **2021**, *264*, 107946. <https://doi.org/10.1016/j.cpc.2021.107946>.
- (54) Kavanagh, S. R.; Squires, A. G.; Nicolson, A.; Mosquera-Lois, I.; Ganose, A. M.; Zhu, B.; Brlec, K.; Walsh, A.; Scanlon, D. O. Doped: Python Toolkit for Robust and Repeatable Charged Defect Supercell Calculations. March 12, 2024. <https://doi.org/10.21105/joss.06433>.
- (55) Kaappa, S.; Malola, S.; Häkkinen, H. Point Group Symmetry Analysis of the Electronic Structure of Bare and Protected Metal Nanocrystals. *J. Phys. Chem. A* **2018**, *122* (43), 8576–8584. <https://doi.org/10.1021/acs.jpca.8b07923>.
- (56) Iraola, M.; Mañes, J. L.; Bradlyn, B.; Horton, M. K.; Neupert, T.; Vergniory, M. G.; Tsirkin, S. S. IrRep: Symmetry Eigenvalues and Irreducible Representations of *Ab Initio* Band Structures. *Computer Physics Communications* **2022**, *272*, 108226. <https://doi.org/10.1016/j.cpc.2021.108226>.
- (57) Gao, J.; Wu, Q.; Persson, C.; Wang, Z. Irvsp: To Obtain Irreducible Representations of Electronic States in the VASP. *Computer Physics Communications* **2021**, *261*, 107760. <https://doi.org/10.1016/j.cpc.2020.107760>.

- (58) Freysoldt, C.; Grabowski, B.; Hickel, T.; Neugebauer, J.; Kresse, G.; Janotti, A.; Van De Walle, C. G. First-Principles Calculations for Point Defects in Solids. *Rev. Mod. Phys.* **2014**, *86* (1), 253–305. <https://doi.org/10.1103/RevModPhys.86.253>.
- (59) Goyal, A.; Gorai, P.; Peng, H.; Lany, S.; Stevanović, V. A Computational Framework for Automation of Point Defect Calculations. *Computational Materials Science* **2017**, *130*, 1–9. <https://doi.org/10.1016/j.commatsci.2016.12.040>.
- (60) Zhang, S. B.; Northrup, J. E. Chemical Potential Dependence of Defect Formation Energies in GaAs: Application to Ga Self-Diffusion. *Phys. Rev. Lett.* **1991**, *67* (17), 2339–2342. <https://doi.org/10.1103/PhysRevLett.67.2339>.
- (61) Freysoldt, C.; Neugebauer, J.; Van de Walle, C. G. Fully Ab Initio Finite-Size Corrections for Charged-Defect Supercell Calculations. *Phys. Rev. Lett.* **2009**, *102* (1), 016402. <https://doi.org/10.1103/PhysRevLett.102.016402>.
- (62) Enkovaara, J.; Rostgaard, C.; Mortensen, J. J.; Chen, J.; Duřak, M.; Ferrighi, L.; Gavnholt, J.; Glinsvad, C.; Haikola, V.; Hansen, H. A.; Kristoffersen, H. H.; Kuisma, M.; Larsen, A. H.; Lehtovaara, L.; Ljungberg, M.; Lopez-Acevedo, O.; Moses, P. G.; Ojanen, J.; Olsen, T.; Petzold, V.; Romero, N. A.; Stausholm-Møller, J.; Strange, M.; Tritsarlis, G. A.; Vanin, M.; Walter, M.; Hammer, B.; Häkkinen, H.; Madsen, G. K. H.; Nieminen, R. M.; Nørskov, J. K.; Puska, M.; Rantala, T. T.; Schiøtz, J.; Thygesen, K. S.; Jacobsen, K. W. Electronic Structure Calculations with GPAW: A Real-Space Implementation of the Projector Augmented-Wave Method. *Journal of Physics: Condensed Matter* **2010**, *22* (25), 253202. <https://doi.org/10.1088/0953-8984/22/25/253202>.
- (63) Mostafanejad, M. Basics of the Spin Hamiltonian Formalism. *International Journal of Quantum Chemistry* **2014**, *114* (22), 1495–1512. <https://doi.org/10.1002/qua.24721>.
- (64) Mosquera-Lois, I.; Kavanagh, S. R.; Walsh, A.; Scanlon, D. O. Identifying the Ground State Structures of Point Defects in Solids. *npj Comput Mater* **2023**, *9* (1), 25. <https://doi.org/10.1038/s41524-023-00973-1>.
- (65) Anand, S.; Toriyama, M. Y.; Wolverton, C.; Haile, S. M.; Snyder, G. J. A Convergent Understanding of Charged Defects. *Acc. Mater. Res.* **2022**, *3* (7), 685–696. <https://doi.org/10.1021/accountsmr.2c00044>.